Acta Biomaterialia 209 (2026) 167–182

Contents lists available at ScienceDirect

Acta Biomaterialia

journal homepage: www.elsevier.com/locate/actbio

Full length article

Dual-orientation of collagen fibers to guide cell alignment in 3D-printed constructs

Diya Singhal [a,1], Fotis Christakopoulos [b,1], Lucia G. Brunel [a], Suraj Borkar [a], Vanessa M. Doulames [b], Esther A.T. Mozipo [c], David Myung [d,e], Gerald G. Fuller [a], Sarah C. Heilshorn [b,*,2]

[a] Stanford University, Department of Chemical Engineering, Stanford, CA, USA
[b] Stanford University, Department of Materials Science and Engineering, Stanford, CA, USA
[c] Stanford University, Department of Bioengineering, Stanford, CA, USA
[d] Stanford University School of Medicine, Department of Ophthalmology, Byers Eye Institute, Palo Alto, CA, USA
[e] VA Palo Alto Healthcare System, Palo Alto, CA, USA

ARTICLE INFO

Dataset link: https://purl.stanford.edu/bw985nr0021, https://doi.org/10.25740/bw985nr0021

Keywords:
Collagen inks
Fiber orientation
Extrusion-based 3D printing
Cell alignment

ABSTRACT

Natural tissue comprises fibrous proteins with complex fiber alignment patterns. Here, we develop a reproducible method to fabricate biomimetic scaffolds with patterned fiber alignment along two independent orientations. While extrusion-based approaches are commonly used to align fibrous polymers in a single orientation parallel to the direction of flow, we hypothesized that extrusion-based 3D printing could be utilized to achieve more complex patterns of fiber alignment. Specifically, we show that control of lateral spreading of a printed filament can induce fiber alignment that is either parallel or perpendicular to the flow direction. Theoretical prediction of the printing parameters that control fiber orientation was experimentally validated using a collagen biomaterial ink. The velocity ratio of the printhead movement relative to the ink extrusion rate was found to dictate collagen fiber alignment, allowing for the informed fabrication of collagen scaffolds with prescribed patterns of fiber alignment. For example, controlled variation of the ink extrusion rate during a single print resulted in scaffolds with specified regions of both parallel and perpendicular collagen fiber alignment. Human corneal mesenchymal stromal cells seeded onto the printed scaffolds adopted a spread morphology that aligned with the underlying collagen fiber patterns. This technique worked well for filaments either printed onto a printbed in air or extruded within a support bath using embedded 3D printing, enabling the fabrication of 3D structures with aligned collagen fibers. Taken together, this work demonstrates a theoretical and experimental framework to achieve the reproducible fabrication of 3D printed structures with controlled collagen fiber patterns that guide cellular alignment.

Statement of Significance

Natural tissues contain collagen fibers aligned in multiple directions, which are essential for guiding cell behavior; however, most existing fabrication methods can achieve only unidirectional fiber alignment. Here, we introduce an extrusion-based 3D printing strategy that enables precise control over collagen fiber orientation in both parallel and perpendicular directions. This allows multidirectional collagen fiber alignment patterned spatially within a single construct, thereby guiding corneal mesenchymal stromal cells to align multidirectionally. This approach works when printing in air or with embedded printing in a support bath. Thus, this strategy can enable the fabrication of complex 3D scaffolds that mimic the anisotropic architecture of native tissues.

* Corresponding author.
E-mail address: heilshorn@stanford.edu (S.C. Heilshorn).

[1] Contributed equally to this work.

[2] Prof. Sarah Heilshorn was an editor of the journal during the review period of the article. To avoid a conflict of interest, Prof. William R. Wagner acted as editor for this manuscript.

https://doi.org/10.1016/j.actbio.2025.11.013
Received 21 June 2025; Received in revised form 21 October 2025; Accepted 10 November 2025
Available online 11 November 2025

1. Introduction

Tissues in the body commonly include a fibrous matrix with exquisite fiber alignment along different directions, which guides cell alignment and spreading [1–9]. The most abundant fibrous protein of the native extracellular matrix (ECM) in the human body is collagen, and varying, complex patterns of collagen fiber alignment are observed across different tissues, such as the cornea, cartilage, and arteries. [5,8,10–13]. For example, in the cornea, the ECM contains orthogonal sheets of collagen fibrils that are able to transmit light while being mechanically resilient [5,14]. In articular cartilage, collagen fibril architecture exhibits depth-dependent organization: fibrils are aligned parallel to the surface in the superficial zone, display a more isotropic distribution in the transitional zone, and orient perpendicular to the surface in the deep zone, where they anchor into the calcified cartilage [12]. This zonal arrangement restricts tissue swelling, facilitates osmotic pressurization for load-bearing, and confers both compressive compliance and shear resistance. Arterial collagen fibers are predominantly arranged in a helical pattern, enabling them to reinforce the artery in both the circumferential and axial directions [13,15].

Collagen fiber alignment can direct many physiological cellular processes, such as migration [16–18], differentiation [6,19], and proliferation [20]. For example, cellular alignment has been widely reported to impact cell proliferation [21], matrix secretion [22,23], and phenotype maintenance [24,25]. Thus, a common goal in tissue engineering is to control the orientation of collagen fibers to guide cell behavior [6,7,16,26]. To date, several fabrication techniques have been used to create substrates with aligned collagen fibers, including electro-spinning, magnetic flow alignment, microfluidics, mechanical strain devices, extrusion through a tapered nozzle, and gravity-based fluidic alignment [6,16,26–29]. While these aligned collagen constructs have been helpful tools to study cell–matrix interactions such as mechanosensing, cell migration speed, and cell persistence, these techniques are typically limited to unidirectional fiber alignment [16,30,31].

Although existing techniques like electrospinning [20,27,32,33] enable nanoscale fiber alignment with high precision, it is typically limited to 2D surfaces or thin scaffolds, lacking structural complexity and spatial control in 3D constructs. Magnetic field-based methods [28,29,33] can orient fibers in 3D hydrogels, but they require incorporation of magnetic nanoparticles or specialized materials, and are constrained by the need for strong, spatially uniform magnetic fields. Shear flow-based alignment, such as induced by microfluidic [29] or controlled extrusion [7,26,34,35], can achieve unidirectional alignment but often lacks the ability to spatially modulate alignment direction within a single filament or print path. Mechanical strain-based methods [9,36], like stretching gels post-printing or during curing, offer bulk alignment but are unsuitable for patterning complex, heterogeneous orientations and often compromise spatial resolution. In addition, many of these conventional approaches rely on discrete, layer-by-layer deposition strategies to alternate fiber alignment direction, which can introduce inter-filamentary gaps and discontinuities while printing complex geometries. Frequent lifting and repositioning of the printhead further interrupts material flow, reducing control over fiber orientation and potentially compromising print fidelity. Creative approaches to overcome these limitations and fabricate radial patterns of collagen fibers have employed Marangoni flow in evaporating, aqueous sessile droplets [37] and microextrusion of discrete filaments in different macroscopic orientations [26]. Yet, it remains challenging to achieve larger constructs with controlled fiber alignment in multiple directions.

3D printing of biological materials has emerged as a reproducible, scalable, and versatile method to fabricate constructs with clinically relevant dimensions and increased complexity [38–45]. In particular, extrusion-based 3D printing offers ease of use and the potential to produce oriented constructs. Alignment in the extrusion direction has been achieved through different methods for a variety of polymers and fibrous materials. For example, alignment can be induced inside the nozzle by subjecting the material to controlled flow profiles during extrusion; alternatively, alignment can be induced outside of the nozzle by subjecting the printed filament to extensional deformation [7,34,35,46–51]. For fibrous collagen inks, shear stress-induced fiber alignment has been achieved through extrusion-based 3D printing, resulting in constructs with uniaxially aligned fibers in the direction of printing [7,26].

Here, we sought to develop an easy to implement and reproducible 3D printing strategy to create constructs with dual-directionally aligned collagen fibers. Specifically, we demonstrate the ability to pattern collagen fibers both parallel to and perpendicular to the printing direction, enabling the fabrication of constructs with more complex patterns of fiber alignment. The primary innovation of this technique lies in its ability to modulate collagen fiber orientation within a single printed filament, enabling transitions between parallel and perpendicular orientations *in situ*. This facilitates the generation of complex, spatially patterned fiber alignments simply by adjusting the printing parameters during continuous extrusion, without the need for changing the printhead trajectory.

To achieve this, we hypothesized that two different printing regimes could be achieved within a single printing setup. The first regime relies primarily on extensional deformation of the collagen ink within a tapered print nozzle to achieve fiber alignment that is parallel to the print direction. In the second regime, we rationalized that controlling the lateral spreading of the printed filament post-printing can be used to induce collagen fiber alignment perpendicular to the printing direction. To explore this idea, we first theoretically predicted how different printing parameters might impact filament lateral spreading. We then performed a systematic evaluation of the printing parameters for our extrusion-based 3D printer and quantified the collagen fiber alignment patterns for each condition. These experimental observations validated our predictions and allowed us to define the printing parameters for each regime of fiber alignment. We next demonstrated the ability of these parallel and perpendicularly aligned collagen substrates to guide the spreading morphology of cells. Using this new printing strategy, we fabricated specimens with dual-directional collagen fiber alignment in a single print. Taken together, this work introduces a predictable, reproducible, and scalable approach to print biomimetic constructs with complex patterns of collagen fiber directionality to guide cellular alignment, while eliminating the need for external fields, complex device modifications, or material additives. The simplicity and compatibility of this method with standard extrusion-based 3D printing make it broadly applicable for engineering tissue-mimetic collagen architectures with high spatial precision.

2. Materials and methods

2.1. Materials

The collagen ink used was the commercial bovine type I neutralized 35 mg mL^{-1} Lifeink 200 (Advanced Biomatrix). Carbopol ETD2020 powder (Lubrizol) was dissolved by rotating overnight at room temperature at 6.94 mg mL^{-1} in 100 mL of sterile, ultrapure deionized water (Millipore) with 0.8 mL of 10 M NaOH (Sigma) to balance the pH to 7. Subsequently, the solution was degassed overnight before use.

2.2. Rheometry

The mechanical properties of the collagen and Carbopol were evaluated through rheological characterization. Small-amplitude oscillatory shear and rotational measurements were performed on an ARG2 rheometer (TA Instruments) equipped with a Peltier plate and a solvent trap to prevent evaporation, using a parallel-plate geometry with a diameter of 8 mm. The absence of wall slip was confirmed through measurements at a different measuring gap having excellent agreement with each other. Collagen gelation was examined through time-sweep

measurements at an angular frequency (ω) of 1 rad s^{-1} and a shear strain amplitude (γ) of 1% at a temperature between 4 °C and 37 °C. Amplitude-sweep measurements were conducted at 4 °C and 23 °C at an angular frequency of 1 rad s^{-1} between a shear strain amplitude of 0.01% and 200%. Frequency-sweep measurements were conducted after the storage modulus (G') had reached a plateau at a shear strain amplitude of 1%, in the linear viscoelastic regime, between an angular frequency of 0.1 and 100 rad s^{-1}. Step-shear measurements were conducted with an alternating shear strain amplitude of 0.1% and 300% using a parallel-plate geometry with a diameter of 8 mm and at an angular frequency of 6 rad s^{-1}. For Carbopol, each shear step lasted 30 s and the measurements took place at room temperature, while for the collagen ink, the low-shear step lasted 300 s and the high-shear step 40 s and the measurements were conducted at 4 °C. Three replicates using a fresh sample were conducted for all measurements.

2.3. 3D printing

3D printing experiments were conducted using a custom-built dual-extruder bioprinter, adapted from a MakerGear M2 Rev E plastic 3D printer, following previously established protocols [41,52,53]. Briefly, the original thermoplastic extruder was replaced with a custom mount supporting two Replistruder 4 syringe pumps, and the control system was upgraded to a Duet 2 WiFi board running RepRapFirmware. For both acellular and cellular printing, the syringe was wrapped with Gel Finger Ice Pack (stored at −20 °C) to retain the collagen at 4 °C, as suggested by the manufacturer. This was done to keep the self-assembly kinetics constant during printing. The printing was performed with nozzles having a diameter of 1.55 mm (14G), 0.84 mm (18G), 0.42 mm (22G), and 0.16 mm (30G) and the plunger distance varied from E = 0.003 mm to E = 0.04 mm. The printing speed (F = 99920 mm min^{-1}), the step distance (Δx = 0.5 mm) and the syringe diameter (D = 7.29 mm) were kept constant for all samples. The entire printing took place in the air at room temperature. Acellular prints were printed as a single 2 cm long filament while the diameter varied ranging from (1 mm to 4.8 mm) depending on the printing parameters. The G-code used was manually written in a text file and no retraction step was included. For prints that were subsequently seeded with cells, the printing process was carried out in a sterile tissue culture cabinet and each sample consisted of three sequentially printed filaments with a length of 2 cm to increase seeding area. All the samples had a thickness of at least 100 μm. Constructs printed in the Carbopol support bath were printed with same printing conditions as in air to allow for comparisons. The 3D structure was printed in Carbopol with hollow features having 9 layered structure. Each layer traced the four walls of a cuboid having length of 3 cm at each wall. The layer height was z = 0.7 mm to ensure good adhesion between the layers. The G-code was designed to have hollow windows inside the 3D structure. Following printing in the Carbopol support bath, the prints were recovered through rigorous washing to ensure complete removal of the support material, followed by thorough PBS rinsing prior to subsequent characterization.

2.4. Cell culture

Human corneal mesenchymal stromal cells (CMSCs) were derived from donor corneal tissue obtained from the Lions Eye Institute for Transplant and Research, following established isolation protocols [54]. The donor, aged 30–35 years, had no recorded history of infections such as herpes simplex virus (HSV), varicella zoster virus (VZV), human immunodeficiency virus (HIV), or hepatitis. The cornea was preserved in Optisol-GS storage medium within seven days postmortem to maintain tissue integrity.

For expansion, cells were cultured in a growth media consisting of Minimum Essential Medium Alpha (MEM-Alpha, Corning) supplemented with 10%v/v fetal bovine serum (FBS, Gibco), 1%v/v GlutaMAX (Gibco), 1%v/v non-essential amino acids (NEAA, Gibco), and 1%v/v antibiotic-antimycotic solution (Gibco) to support cell proliferation and minimize contamination. The growth media changes were performed every 48 h. Once cultures reached approximately 80% confluency, CMSCs were passaged using standard enzymatic dissociation techniques. All experiments were conducted using cells between passages 6 and 10 to maintain cellular consistency and avoid senescence-related effects. For all the cell experiments in this study, the cells were seeded on the bottom side of the print, as it is flatter than the top side of the print. To achieve this, first, the prints were flipped in PBS solution to avoid the prints from breaking and subsequqntly the PBS solution was pipetted out. Then, CMSCs were trypsinized, counted, pelleted, re-suspended in media, and seeded at an initial cell density of 10^4 cells cm^{-2} onto the flipped prints.

2.5. In vitro characterization

To evaluate CMSC viability, a Live/Dead viability assay was performed using calcein-AM and ethidium homodimer-1 (EthD-1) staining, following the manufacturer's protocol (Life Technologies). Cells were incubated for 15 min at 37 °C in a staining solution composed of 0.6 μL calcein-AM and 2 μL EthD-1 per 1 mL of PBS. Following staining, samples were imaged using a STELLARIS 5 confocal microscope (Leica) equipped with a 10× air objective to visualize live (green) and dead (red) cells. At least five images were taken in different areas of each print, and image analysis was performed using FIJI (ImageJ2, Version 2.3.0/1.53f). Cell viability was calculated as the number of live cells (calcein AM-positive) divided by the total number of cells.

For immunofluorescence analysis, prints with seeded CMSCs were fixed in 4% paraformaldehyde (PFA) prepared in PBS for 20 min at room temperature (RT), followed by three PBS washes of 10 min each. Permeabilization was carried out using 0.25% Triton X-100 (Sigma Aldrich) in PBS (PBST) for 45 min at RT. Samples were then incubated for 2 h at RT in a blocking solution consisting of PBS supplemented with 5 wt% bovine serum albumin (BSA; Roche), 5% goat serum (Gibco), and 0.5% Triton X-100 to reduce nonspecific binding.

Primary and secondary antibodies were diluted in an antibody solution consisting of PBS supplemented with 2.5 wt% BSA, 2.5% goat serum, and 0.5% Triton X-100. Samples were incubated overnight at 4 °C with rabbit anti-ALDH-3A1 primary antibody (Abcam, ab76976) at a 1:200 dilution. The following day, excess antibody was removed by three 20-minute washes in PBST. Secondary labeling was performed using a solution containing DAPI (1:900; Molecular Probes), phalloidin–tetramethylrhodamine B isothiocyanate (Phalloidin-TRITC; Sigma Aldrich, 1:1000), and Alexa Fluor 488-conjugated goat anti-rabbit secondary antibody (1:500), all diluted in the antibody solution. Samples were incubated with this solution overnight at 4 °C.

After staining, samples were washed three times in PBST and imaged using a STELLARIS 5 confocal microscope (Leica) equipped with 10× air and 40× oil immersion objectives. Imaging was performed using tile scanning mode with a resolution of 512 × 512 pixels.

2.6. Microscopy

Collagen fibers in the acellular prints were imaged with a STELLARIS 5 confocal microscope (Leica) using a 40× oil objective. Tile scans were taken at 512 × 512 image format for the entire print. Images were acquired up to 60 μm from the bottom of the sample.

Second harmonic generation (SHG) microscopy was conducted on an inverted Nikon Ti2-E microscope with a C2 confocal scanner. Nikon CFI Apochromat TIRF 40X air objective was used for imaging. A sliding mirror (Optique Peter) allowed for easy alternation between confocal fluorescence and SHG excitation modalities. For SHG, a picosecond-pulsed laser system (picoEmerald S, APE America Inc.) emitting 2 ps pulses at an 80 MHz repetition rate and with a 10 cm^{-1} spectral bandwidth was used. The system consists of a tunable optical parametric oscillator (700–960 nm) pumped at 1031 nm by an ytterbium fiber

laser. The oscillator was set to 797 nm, generating an SHG signal at 398.5 nm. The emitted signal was routed through optical filters (BrightLine 400/12, Thorlabs 390/18, and Thorlabs FESH0500) before detection by a photomultiplier tube (Hamamatsu R6357). The laser power at the sample was 500 mW. To facilitate imaging, samples were printed onto glass coverslips (BRAND) and PAP pen barrier drawn around print with 100 μL PBS added to avoid drying. Five distinct regions were imaged per sample, each captured as a 5×4 μm tile scan. Images were acquired at 1024×1024 pixels (75.3×75.3 nm pixel^{-1}) with a dwell time of 10.8 μs pixel^{-1}.

Scanning electron microscopy micrographs were acquired using a ThermoFisher Apreo SEM (3 kV, 50 pA) using in-lens detectors. Dried prints were coated with 3 nm of Au/Pd.

2.7. Image analysis

Confocal images were analyzed to characterize collagen fiber alignment qualitatively and quantitatively. For qualitative analysis, CT-FIRE for Individual Fiber Extraction software was used to enable automated tracing of the collagen fibers by artificially coloring individual fibers to aid in visual assessment of the overall collagen fiber alignment in the sample [55]. For quantitative analysis, confocal images were analyzed using the Orientation J plugin in FIJI (Image J) software. The fraction of fibers corresponding to each orientation was obtained as a function of orientation angle (in degrees, °). Using this, histograms of normalized frequency of fibers relative to the total number of fibers versus orientation angle were plotted with bins of 20°.

Collagen reflectance images were also analyzed through CT-FIRE MATLAB software to quantify fiber dimensions (width). Three independent printing trials were analyzed for each experimental condition and plotted as mean ± standard deviation.

To perform fast Fourier transform (FFT) analysis, confocal reflectance and SHG images were analyzed in ImageJ software using the oval profile plug-in. The FFT function was applied to transform image data from real space into frequency space, generating FFT output images. A circular projection was then placed on each FFT output, and pixel intensities were radially summed at 1.2° increments between 0° and 360°. Because the FFT is symmetric, only values between 0° and 180° were plotted. To account for the inherent mathematical transformation of the FFT, datasets were rotated by 90° to allow direct determination of the principal orientation. Finally, pixel intensity values were normalized to a baseline of 0 and plotted in arbitrary units, enabling cross-comparison between datasets.

Cellular alignment of the seeded CMSCs on the gels was analyzed with CellProfiler, an open-source software using confocal images of the cells visualized with calcein-AM (live) stain. The color code was generated by modifying the color survey javascript code in the Orientation J plugin code file and remerged with the ImageJ software package to perform the analysis.

2.8. D^*, V^* and AP calculation and workflow

The workflow for the measurement and analysis of the alignment started by defining the Alignment parameter (AP). The AP is defined as the ratio of the fraction of perpendicular fibers (orientation ranges from −80° to −60° and 60° to 80°) to the fraction of parallel fibers (orientation from −20° to 20°) in the print. To get the fractions, the confocal images of the print were analyzed through the OrientationJ plugin in ImageJ software. A histogram of the normalized frequency of fibers for different orientations of the fibers (ranging from −90° to 90°) was generated. We created bins of 20° gaps. Then, by using the y-axis values for the angles (−80°, −60°, 60°, 80°), the fraction of perpendicular aligned fibers in the sample was determined. Similarly, by using the y-axis values from −20°, 0°, 20°, the fraction of parallel aligned fibers in the sample was determined, providing an estimate for the Alignment Parameter for each printing condition.

Then, different regimes of alignment direction were defined based on the AP values. A threshhold of 0.5 was chosen for parallel alignment as it means that the amount of fibers in the parallel direction are at least double that of the amount of fibers in perpendicular direction. Through a similar analysis, for perpendicular alignment, a threshhold of 2 for AP was chosen. The range between 0.5 to 2 was defined as random alignment since there is no preferential direction of fiber alignment.

To understand the physical significance behind achieving different alignment directions for different printing conditions, we defined the quantity D^* (diameter ratio) as the ratio of the diameter of printed filament (after printing on the printbed) to the diameter of the nozzle. The perpendicular alignment of fibers can be correlated to the spreading of the printed filament relative to the nozzle diameter it is printed from. Particularly, when $D^* > 1$, the diameter of the printed filament is greater than the diameter of the nozzle, leading to lateral spreading and aligning fibers perpendicular to the printing direction. In contrast, when $D^* \leq 1$, the diameter of printed filament is less than or equal to the nozzle diameter, leading to filament stretching and aligning fibers parallel to the printing direction. Moreover, the experimental printing conditions that lie within $AP \leq 0.5$ or the parallel regime, collectively fall in the regime of $D^* \leq 1$. The reasoning is identical for the cutoff of $1 < D^* \leq 2$ and $D^* > 2$ for random and perpendicular alignment regimes, respectively.

To develop a generalized parameter that depends solely on printing conditions and can serve as a guideline for controlling fiber alignment, we defined velocity ratio (V^*) as the ratio of the speed of the ink extrusion from the nozzle to the translational speed of the printhead. Based on the threshold values of AP, we observed that the experimental conditions within the parallel alignment regime $AP \leq 0.5$ or the parallel regime, collectively fall in the regime of $V^* \leq 0.5$. Similarly, the experimental printing conditions that lie within $AP > 2$ or the perpendicular regime, collectively fall in the regime of $V^* > 1$. These regimes for V^* have physical significance as when $V^* > 1$, *i.e.* the speed at which ink is extruded is higher than the translational speed of the printhead, the ink would experience significant lateral spreading on the printbed, leading to perpendicular fiber alignment relative to the printing direction. In contrast, when $V^* \ll 1$, *i.e.* the speed at which the ink is extruded is lower than the translational speed of the printhead, the filament will become extensionally drawn as it gets extruded, leading to parallel fiber alignment.

2.9. Statistical analysis and fitting

Statistical analysis was performed using GraphPad Prism (Version 10). For the comparison of the printed filament diameter (d_{print}) across different E and nozzle dianeters (d_{nozzle}), a two-way analysis of variance (ANOVA) with Tukey's multiple comparisons test was used. For Table S3, the theoretical curves of D^* for different d_{nozzle} and for a range of E values are fitted with experimental data points to find the fitted value of β using the fmincon feature in MATLAB. The experimental and fitted theoretical points are plotted together to calculate the goodness of fit as R^2.

Specific details of each statistical analysis are presented in the figure captions. In all cases, $N \geq 3$ independent gels for each condition. In all cases, statistical differences are denoted as follows: not significant (ns, $p > 0.05$), ($^*p < 0.05$), ($^{**}p < 0.01$), ($^{***}p < 0.001$), ($^{****}p < 0.0001$). Data are presented as mean ± standard deviation unless specified otherwise.

3. Results and discussion

3.1. Collagen fiber alignment along the printing direction

Collagen inks are widely used in 3D printing, both in the solution and the gel state [7,10,56,57]. Collagen gelation is attained through physical assembly and entanglement of collagen fibers at physiological

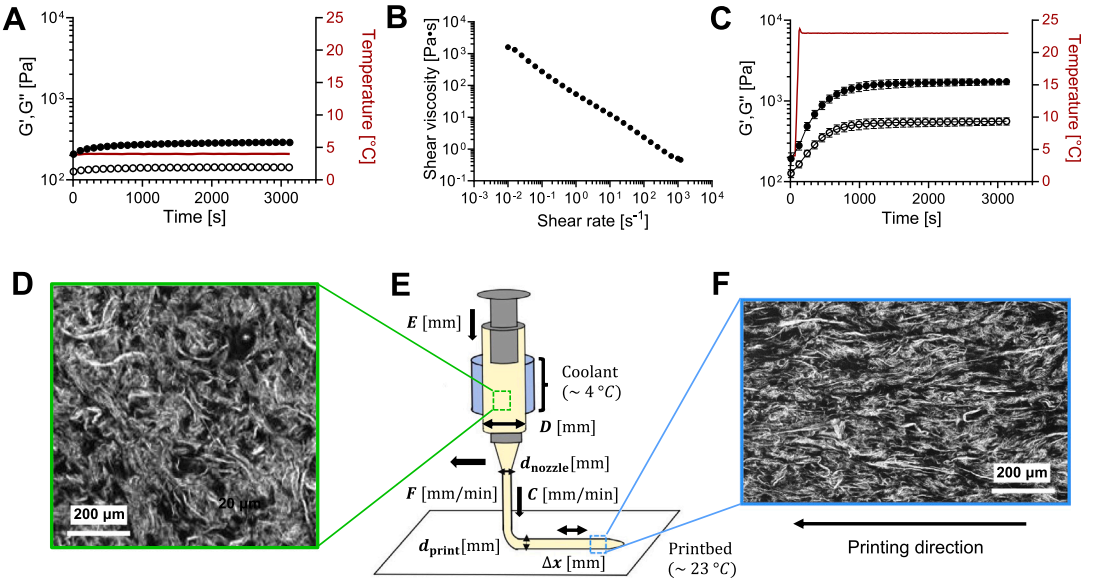

Fig. 1. Extrusion-based 3D printing setup for collagen fiber alignment. (A) Time sweep, shear rheology of the collagen ink at 4 °C; (storage modulus, G', •; loss modulus, G'', ∘; temperature: red solid line). (B) Shear-dependent viscosity of the collagen ink at 4 °C. (C) Shear rheology of the collagen ink as temperature increases from 4 °C to 23 °C; (storage modulus, G', •; loss modulus, G'', ∘; temperature: red solid line). (A–C) Data are mean ± standard deviation; $N = 3$ independent gels. For (A) and (B), symbol size is larger than the error bars. (D) Representative confocal reflectance image of the collagen ink prior to extrusion. (E) Schematic of the extrusion-based printing setup showing the different printing parameters; ink cartridge diameter (D, mm), nozzle diameter (d_{nozzle}, mm), translational speed of the printhead (F, mm min^{-1}), speed of ink extrusion (C, mm min^{-1}), plunger displacement per step (E, mm), lateral displacement distance of the printhead per step (Δx, mm), and diameter of the printed filament (d_{print}). An ice pack is positioned around the syringe to keep the ink at 4 °C, which is deposited on a printbed in air at room temperature. (F) Representative confocal reflectance image of the collagen post-printing, showing fiber alignment parallel to the printing direction (black arrow). (For interpretation of the references to color in this figure legend, the reader is referred to the web version of this article.)

conditions, with the kinetics being dependent on collagen concentration, temperature, and pH [58–61]. Collagen inks have been formulated to form fibers before printing, during printing, or after printing [10]. We chose to formulate a collagen ink with pre-formed fibers that would become oriented by fluid mechanics, as we reasoned that printing parameters would have a stronger impact on pre-formed fibers as opposed to soluble collagen protein [62]. Specifically, we selected a neutralized type-I atelocollagen at a relatively high concentration of 35 mg mL^{-1} that is stored and printed at 4 °C. At these conditions, the ink has storage (G') and loss (G'') moduli of about 250 Pa and 150 Pa, respectively (Fig. 1(A), supplemental figure S1(A)). Thus, the ink is already a weak gel ($G' > G''$) prior to printing, due to its high concentration and neutral pH. Importantly, the ink at 4 °C displays shear-thinning behavior, making it suitable for extrusion-based 3D printing (Fig. 1(B)). Additionally, this ink formulation demonstrates the ability to recover after shear-thinning. After exposure to high shear that disrupts the network structure, the fluid achieves an 80% storage modulus recovery in 30 s at 4 °C and recovers its initial stiffness after 240 s (supplemental figure S1(B)). As the ink is deposited on the printbed at room temperature, the physical assembly of the collagen fibers continues to progress, as evident in the ten-fold increase in G', reaching a plateau of 2000 Pa and a yield stress of 57 Pa (Fig. 1(C), supplemental figure S1(C)). The presence of fibers in the ink cartridge was confirmed by confocal reflectance microscopy at 4 °C (Fig. 1(D)). As expected, collagen fibers within the ink are initially randomly oriented.

To demonstrate that this collagen ink could achieve parallel alignment similar to that reported by others [7], we employed a standard extrusion-based 3D printing system (Fig. 1(E)). This setup offers several user-defined parameters including the ink cartridge diameter, D, which we kept constant through all experiments (7.29 mm), and the diameter of the printing nozzle, d_{nozzle}, which was varied in our studies. In addition to these hardware parameters, the setup also includes a number of user-defined parameters controlled through the software (*e.g.* Gcode). These include the plunger displacement per step, E, the lateral displacement of the printhead per step, Δx, and the translation speed of the printhead, F. Here, we use a tapered nozzle to promote parallel fiber alignment inside the printing nozzle through an applied extrusion draw ratio, resulting in elongational deformation. Through these hardware- and software-controlled variables, we define further printing parameters such as the speed of ink extrusion from the nozzle, C, and the diameter of the printed filament, d_{print}. Through optimization, we were able to identify a combination of printing parameters (supplemental table S1) that results in parallel fiber alignment within the printed filament at 23 °C (Fig. 1(F)), similar to results of others [7]. Filament height after printing will vary depending on the nozzle diameter and printing conditions. The thickness of the constructs printed in this work ranged from 500–800 µm. Upon further heating of the collagen print to physiological temperature (37 °C), additional collagen fiber formation occurs, as evidenced by a further increase in G' to about 3500 Pa (supplemental figure S1(D,E)). To confirm that the heating to 37 °C does not disrupt the achieved fiber alignment, we incubated the sample for 15 min and then confirmed that the alignment remains unchanged by confocal reflectance imaging (supplemental figure S1(F)). Analysis of the fiber geometry shows that the final collagen fibers have a diameter of 6.33 ±1.14 µm (supplemental figure S2(A)), similar to reports from others [63,64]. In addition, scanning electron microscopy of the aligned fibers confirms that the individual fibers are composed of self-assembled fibrils (supplemental figure S2(B)), as expected [65]. Having been able to replicate the state of the art with our extrusion-based 3D printing setup, we next investigated the ability to achieve fiber alignment in an orientation other than the printing direction, towards the broader goal of fabricating constructs with dual-directional collagen fiber alignment.

3.2. Printed filament spreading dictates fiber alignment orientation

Previously, an interesting correlation between extruded width and fiber alignment had been shown where low extrusion width leads

to more fibers aligned in the printing direction, while as extruded width increases, less fibers are aligned in the printing direction [66]. We hypothesized that harnessing the lateral spreading of the printed filament post-printing would lead to perpendicular alignment of the collagen fibers. This lateral spreading of the printed filament can be quantified as a ratio of the printed filament diameter (d_{print}) to the nozzle diameter (d_{nozzle}), which we define as the diameter ratio, D^*, (supplemental figure S3):

$$D^* = \frac{d_{print}}{d_{nozzle}}. \quad (1)$$

Thus, when $D^* < 1$, the printed filament diameter is smaller than the nozzle diameter, implying less printed filament spreading. In contrast, when $D^* > 1$, the printed filament diameter is higher than the nozzle diameter, denoting more printed filament spreading. To control the lateral spreading of the printed filament, we derived a theoretical expression of D^* by performing a mass balance. For our extrusion-based, piston-controlled, 3D printer, the volumetric flow rate inside the syringe ($\dot{Q}_{syringe}$) is defined as:

$$\dot{Q}_{syringe} = \frac{A_{syringe} E}{\frac{\Delta x}{F}}, \quad (2)$$

which, due to mass conservation, is equal to the volumetric flow rate at the end of the nozzle ($\dot{Q}_{nozzle}$):

$$\dot{Q}_{nozzle} = \dot{Q}_{syringe}. \quad (3)$$

Similarly, the volumetric flow rate at the end of the nozzle can be equated to that of the printed filament after extrusion from the nozzle ($\dot{Q}_{filament}$):

$$\dot{Q}_{nozzle} = \dot{Q}_{filament}. \quad (4)$$

We initially assume the printed filament is a cylinder to enable the estimation of $\dot{Q}_{filament}$ as:

$$\dot{Q}_{filament} = \frac{F \pi d_{print}^2}{4}. \quad (5)$$

In actuality, the printed filament will not be a perfect cylinder, and to account for this, we introduce the coefficient, β. When $\beta = 1$, then the cross-section of the printed filament would be perfectly circular (*i.e.* the width and height of the printed filament will be similar), and when $\beta > 1$, the filament will undergo lateral spreading.

Using conservation of mass, through Eq. (2)–(5) we find:

$$\frac{A_{syringe} E}{\frac{\Delta x}{F}} = \frac{F \beta \pi d_{print}^2}{4} \quad (6)$$

giving us a theoretical prediction for d_{print} as:

$$d_{print} = \sqrt{\frac{4 \beta A_{syringe} E}{\pi \Delta x}} \quad (7)$$

In turn, D^* (*i.e.* the normalized printed filament diameter) can also be correlated to the printing parameters as:

$$D^* = \frac{1}{d_{nozzle}} \sqrt{\frac{4 \beta A_{syringe} E}{\pi \Delta x}} \quad (8)$$

From Eq. (8), it can be duly noted that D^* depends on two of the printing parameters introduced in Fig. 1(E), namely E (plunger distance per step) and d_{nozzle} (nozzle diameter), with the proportionality given as:

$$D^* \propto \frac{\sqrt{E}}{d_{nozzle}} \quad (9)$$

To test this theoretical prediction, we conducted a series of controlled experiments where either E or d_{nozzle} was independently varied. For each experimental condition, we measured the actual d_{print} (*i.e.* the printed filament width) through confocal imaging to calculate an experimentally observed D^*. First, we kept E constant ($E = 0.007$ mm) and decreased d_{nozzle} from 1.55 mm to 0.16 mm (a ratio of $\simeq$ 9.7:1). Upon microscopy analysis of the resulting printed filaments, we observed that decreasing d_{nozzle} causes D^* to increase from 0.875 to 8.406 (a ratio of $\simeq$ 1:9.6) (Fig. 2(A)). Thus, for these conditions, we found that D^* and d_{nozzle} are inversely proportional, consistent with our theoretical prediction (Eq. (9), supplemental figure S4).

Next, we kept d_{nozzle} constant ($d_{nozzle} = 1.55$ mm) while E was increased from 0.005 mm to 0.040 mm (a ratio of $\simeq$ 1:8) (Fig. 2(B)). Upon measuring the width of the printed filament for increasing E, we observed that D^* increased from 0.875 to 3.019 (a ratio of $\simeq$ 1:3.45). Thus, these experimental results are consistent with our theoretical prediction that D^* is directly proportional to $\sqrt{E}$ (Eq. (9)).

After validating our ability to predict the printed filament width based on our printing parameters, we then observed the fiber alignment within each filament using confocal reflectance microscopy. To aid in the assessment of fiber alignment direction and to prevent observational bias, we used an automated fiber tracing algorithm (CT-FIRE for Individual Fiber Extraction) [55] that traces and artificially colors individual fibers to enable visualization of fiber orientation (supplemental figure S5). In addition, we performed two-dimensional fast Fourier Transform analysis on representative confocal reflectance and second harmonic generation (SHG) images to confirm the identified fiber alignment (supplemental figures S6, S7). All three characterization methods provided similar results, thus we continued with the automated fiber tracing algorithm, which provides intuitive visualization. We found that at low D^* (*i.e.* the condition where uniaxial filament extension occurs, 0.875 in the left panels in Fig. 2(A,B)), the collagen fibers were oriented parallel to the printing direction (supplemental figure S5).

In contrast, for the conditions with $D^* > 1$ (*i.e.* significant lateral filament spreading, 8.406 and 3.019 in the right panels of Fig. 2(A) and 2(B), respectively) the collagen fibers were observed to orient perpendicular to the filament printing direction (supplemental figure S5). Here, despite use of the same tapered nozzle that produced parallel fiber alignment in our earlier experiments (Fig. 1), we observed perpendicular fiber alignment for smaller nozzle diameters, which will impart greater nozzle shear stress (Fig. 2 and supplemental figure S5). Thus, if parallel fiber alignment occurs within the nozzle, the printed collagen ink still retains sufficient fluidity to allow for fiber reorientation into a perpendicular alignment in response to fluid forces during lateral spreading. This observation is consistent with our hypothesis that fluid flow that occurs after extrusion while the filament is undergoing uniaxial extension or lateral spreading can be sufficient to induce parallel or perpendicular alignment of embedded collagen fibers, respectively. For experimental conditions with an intermediate value of D^* ($D^* \simeq 1$, middle panels of Fig. 2(A,B)), the collagen fibers were randomly oriented (supplemental figure S5). This observation suggests that there is an intermediate transition regime where the embedded fibers experience neither sufficient extensional flow to orient in the parallel direction, nor enough lateral flow to orient perpendicularly.

3.3. Quantification of fiber alignment across a broad printing space

We next wanted to identify the relevant values of D^* to achieve parallel or perpendicular collagen fiber alignment across a wide range of printing parameter space. To categorize the prints into different alignment regimes, we developed a technique to quantify the fiber alignment orientation using the Orientation J plugin in FIJI (Image J) software from the confocal reflectance micrographs (Fig. 3(A)). From this analysis, we prepared histograms showing the normalized frequency of fiber alignment relative to the total number of fibers versus fiber orientation, where the printing direction is 0° (Fig. 3(B, C) and supplemental figures S8(B), S9(A,B)).

From these histograms, we further calculated an Alignment Parameter (*AP*), which we define as the ratio of the fraction of perpendicular fibers (orientation ranges from −80° to −60° and 60° to 80°) to the fraction of parallel fibers (orientation from −20° to 20°). To support visual

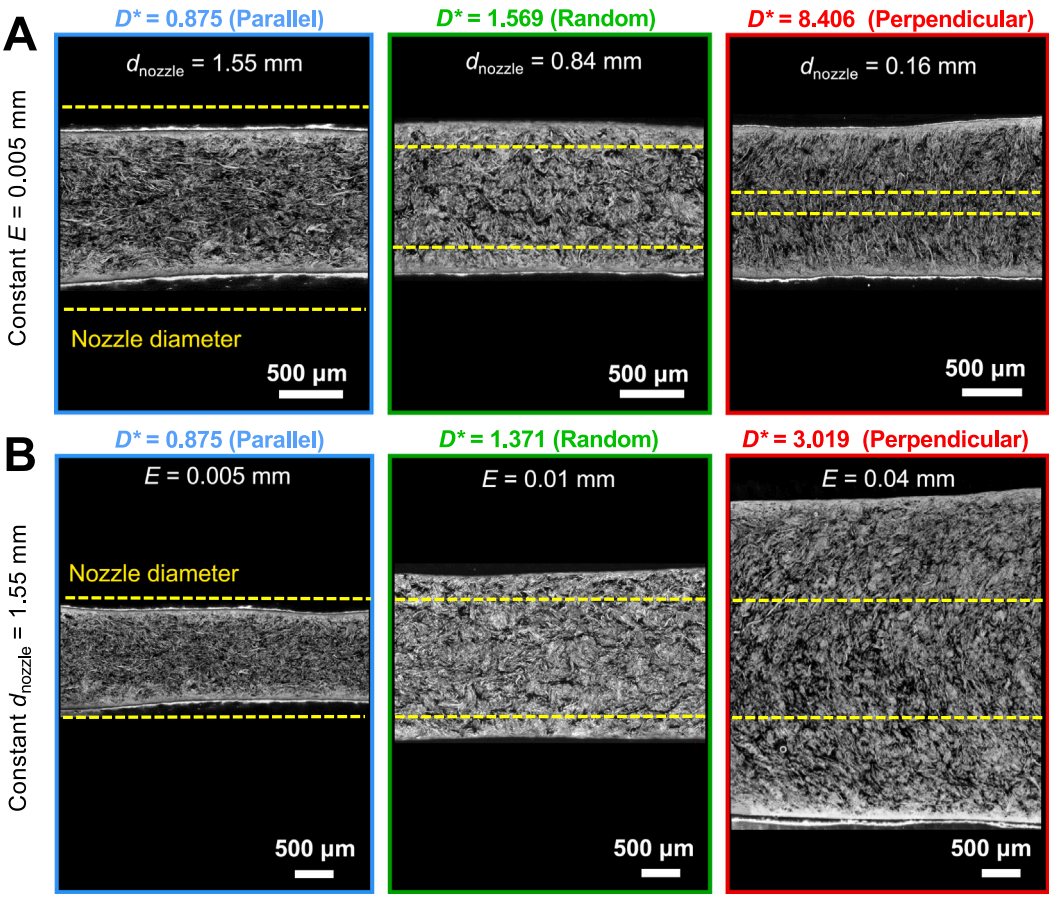

Fig. 2. Diameter ratio correlates with collagen fiber alignment in printed filaments. (A) Representative confocal reflectance images of collagen filaments printed with the same plunger displacement per step (E = 0.005 mm) and different nozzle diameters (d_{nozzle}). (B) Collagen filaments printed with the same nozzle (d_{nozzle} = 1.55 mm) and different plunger displacement per step (E). Yellow dotted lines denote the nozzle diameter for easy comparison to the printed filament width. The experimentally determined diameter ratio, D^*, (*i.e.* the width of the printed filament, d_{print}, normalized by the diameter of the printing nozzle, d_{nozzle}) is written above each micrograph along with a qualitative description of the observed collagen fiber orientation. Scale bars correspond to 500 µm. (For interpretation of the references to color in this figure legend, the reader is referred to the web version of this article.)

validation of our automated analysis, we also used the aforementioned automated fiber tracing algorithm to artificially color individual fibers (Fig. 3(A)). With this analytical workflow in place, we systematically varied E and d_{nozzle} and quantified the fiber alignment for three independent printing trials at each of the 24 conditions (supplemental table S2). First, we found that by keeping d_{nozzle} constant (d_{nozzle} = 1.55 mm or 0.84 mm, left and middle columns, respectively, in Fig. 3(A)), the fiber alignment direction can be transitioned from parallel to random to perpendicular by increasing the plunger displacement E from 0.003 mm to 0.04 mm (left and middle graph in Fig. 3(A,B)). Interestingly, for choice of smaller d_{nozzle} (0.16 mm, right-most column, (Fig. 3(A)) or 0.42 mm (supplemental figure S8(A)), the fiber alignment direction was predominantly perpendicular for all E values tested (right column in Fig. 3(A,B) and supplemental figure S8(B)). These data suggest that careful selection of a single nozzle could be used to print all three different fiber orientations within a single construct.

An alternative method to control the fiber alignment orientation is to keep E constant while varying d_{nozzle}. For lower E values (0.003 or 0.007 mm, top two rows in Fig. 3(A)), decreasing d_{nozzle} from 1.55 to 0.16 mm resulted in a transition from parallel to perpendicular fiber alignment, respectively (top two graphs in Fig. 3(C) and supplemental figure S9(A)). For larger E (0.01 mm or 0.04 mm, bottom two rows in Fig. 3(A)), the alignment direction is predominantly perpendicular for all d_{nozzle} values (bottom graph in Fig. 3(C)) and supplemental figure S9(B)). These data suggest that multinozzle printing systems also could be used to achieve all three different fiber orientations within a single construct.

To synthesize together the information from each histogram into a single quantitative metric, we next calculated and plotted the AP value for each of the 24 tested combinations of printing parameters (Fig. 3(D), supplemental table S2). This allowed us to identify cutoff values of AP that define the three regions of fiber alignment: parallel (blue, $AP \leq 0.5$), random (green, $0.5 < AP \leq 2$), and perpendicular (red, $AP > 2$) (Fig. 3(D)). At the cutoff value of $AP \leq 0.5$, the number of fibers aligned in the parallel direction is approximately twice that of the perpendicular direction. In the green, random region ($0.5 < AP \leq 2$), the proportions of parallel and perpendicular fibers are comparable. Finally, for $AP > 2$, roughly twice as many fibers are oriented perpendicularly compared to those aligned in the parallel direction. Interestingly, for this particular ink formulation and printer setup, we found that 16 of the 24 tested printing parameter combinations resulted in perpendicular fiber alignment (Fig. 3(D), supplemental table S2). Thus, while most bioprinting studies to date have focused on the parallel alignment of fibers, our printing strategy enables to readily achieve perpendicular fiber alignment through multiple combinations of E and d_{nozzle}.

3.4. Normalized speed of ink extrusion dictates fiber alignment orientation

Although the exact values of E and d_{nozzle} that result in perpendicular or parallel fibers will be different for each printer setup, we reasoned

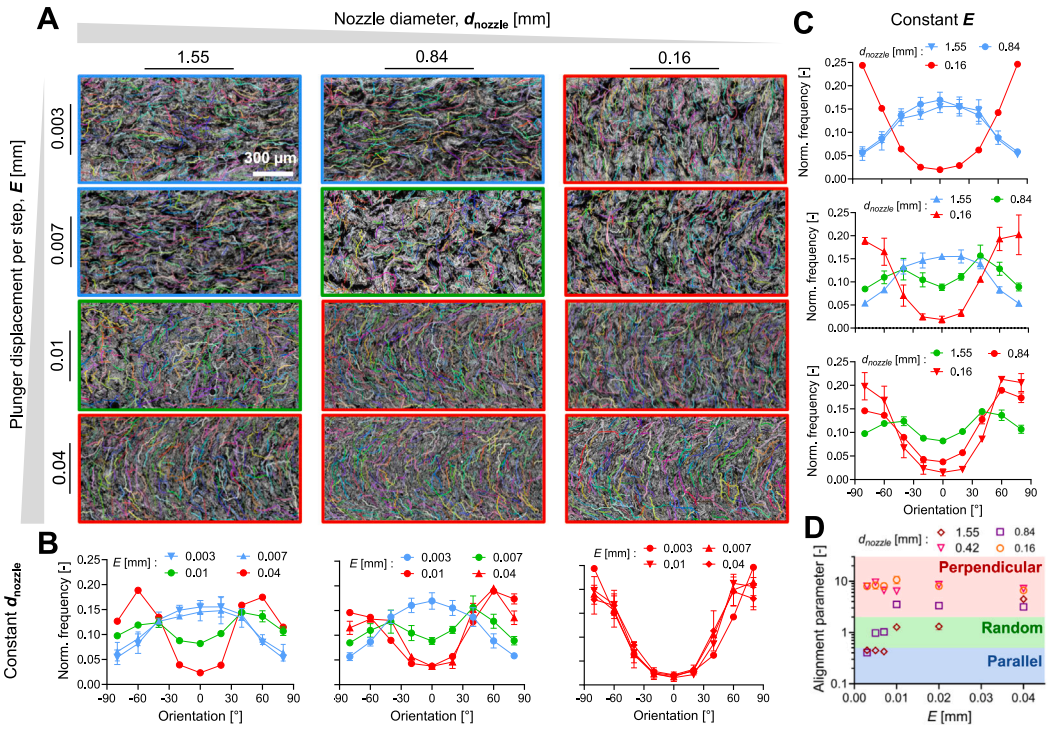

Fig. 3. Selection of printing parameters controls the collagen fiber alignment direction. (A) Automated analysis of representative confocal reflectance images for different combinations of plunger displacement per step (E) and nozzle diameter (d_{nozzle}) leads to identification of parallel (blue), random (green), and perpendicular (red) alignment regimes. (B) Histograms of fiber alignment when keeping the nozzle diameter constant (at d_{nozzle} = 1.55 mm, d_{nozzle} = 0.84 mm, d_{nozzle} = 0.16 mm, from left to right graph respectively) and changing the plunger displacement, showing the normalized frequency of fiber alignment relative to the total number of fibers versus fiber orientation, where the printing direction is 0°. (C) Histograms of fiber alignment when keeping the plunger displacement constant (at $E = 0.003$ mm, $E = 0.007$ mm and $E = 0.01$ mm, from top to bottom graph respectively) and changing the nozzle diameter. (D) Alignment parameter (AP) plotted for several combinations of E and d_{nozzle} show that the printing parameter space can be divided into three regimes with different fiber alignment directions: parallel (blue, $AP \leq 0.5$), random (green, $0.5 < AP \leq 2$), and perpendicular (red, $AP > 2$). (B, C) Data are mean ± standard deviation, $N = 3$ independent printing trials. (For interpretation of the references to color in this figure legend, the reader is referred to the web version of this article.)

that more generalizable guidelines could be identified by considering how AP relates to the D^* ratio as defined previously in Eq. (8). Towards this goal, we first experimentally identified the dependence of E and d_{nozzle} on the printed filament width (d_{print}). As E increases from 0.003 to 0.04 mm, d_{print} increases monotonically due to the increased amount of extruded material. Interestingly, we observed that for a particular E value, d_{print} remains the same irrespective of d_{nozzle} (Fig. 4(A)), which is consistent with our theoretical prediction (Eq. (7)). By plotting AP against D^* for our 24 printing conditions, we were able to identify the ranges of D^* for the three fiber alignment regimes using our earlier AP cutoff values (Fig. 4(B), supplemental table S2). Specifically, we found that $D^* \leq 1$ produced filaments in the parallel fiber alignment region ($AP \leq 0.5$), and $D^* > 2$ produced filaments in the perpendicular fiber alignment region ($AP > 2$). For values between these two regions, *i.e.* $1 < D^* \leq 2$, fibers had random alignment.

We then compared the experimentally determined values of D^* to our earlier theoretical prediction (Eq. (8)), where the only fitting parameter is β (Fig. 4(C)). When fitting our experimental data to this equation, we found the same value of $\beta = 4.49 \pm 0.031$ (supplemental table S3) for each d_{nozzle} tested across the full range of E. This constant fitting parameter further supports the notion that β is a material dependent parameter that does not change with the tested printing conditions, and thus remains unchanged for a given ink and substrate system (*e.g.* ink composition, pH, temperature, and printbed surface).

To reformulate our theoretical prediction into a format that is independent of β, so that it is controlled solely by the experimental printing parameters (*e.g.* E, d_{nozzle}, F, D, Δx) for a specific ink system, we defined the normalized velocity, V^*:

$$V^* = \frac{C}{F} \tag{10}$$

where C corresponds to the speed of the ink extrusion from the nozzle and F to the translational speed of the printhead. We hypothesized that when $C \gg F$, *i.e.* the speed at which the ink is extruded is higher than the translational speed of the printhead, the ink would experience significant lateral spreading on the printbed, leading to perpendicular fiber alignment relative to the printing direction (Fig. 4(D)). In contrast, when $C \ll F$, *i.e.* the speed at which the ink is extruded is lower than the translational speed of the printhead, the filament will become extensionally drawn as it gets extruded, leading to parallel fiber alignment. When $C \approx F$, *i.e.* the speed at which the ink is extruded is comparable to the translational speed of the printhead, the filament does not experience significant lateral spreading or extensional drawing, leading to random alignment of fibers.

This normalized velocity framework enables extension to other extrusion-based systems such as pneumatic-controlled printers, where F is explicitly selected, while C will depend on the pressure drop through the syringe and nozzle, ΔP. The maximum stress, τ_w in capillary flow can be calculated from: [67]

$$\tau_w = \frac{d_{nozzle}\Delta P}{4L}, \tag{11}$$

where L is the length of the nozzle. For power-law fluids, the shear rate, $\dot{\gamma}_w$, is calculated from:

$$\dot{\gamma}_w = \frac{3n+1}{4n} \cdot \frac{32\dot{Q}}{\pi d^3_{nozzle}}, \tag{12}$$

where n is the power-law index. Through supplemental equation (S4) and:

$$\tau_w = \eta\dot{\gamma}_w, \tag{13}$$

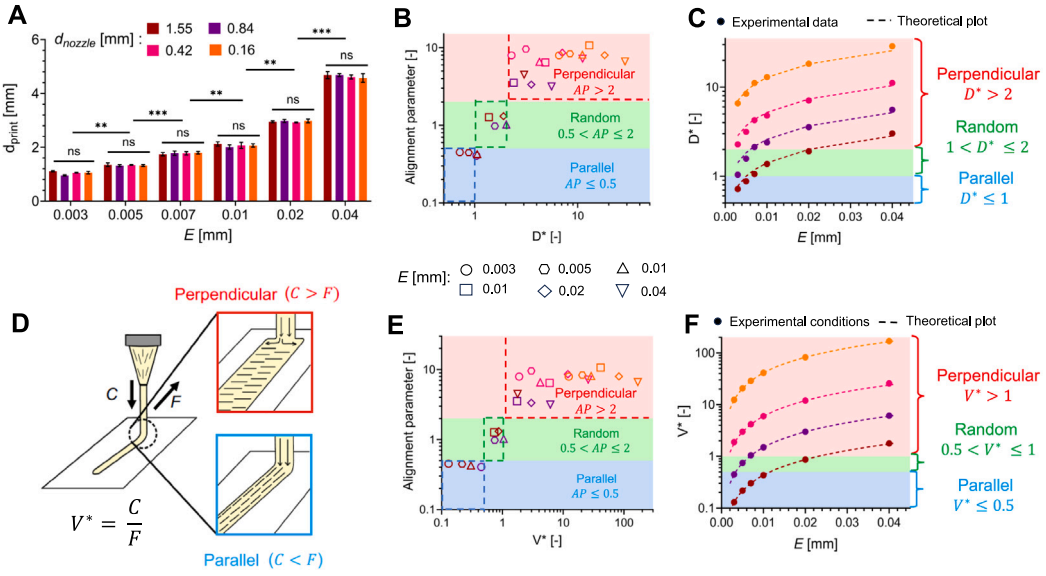

Fig. 4. Relative speed of ink deposition controls filament spreading and fiber alignment. (A) Experimentally determined printed filament width (d_{print}) plotted as a function of E for different values of d_{nozzle}. Symbol colors denote d_{nozzle}, while symbol shapes denote E. (B) Alignment parameter (AP) plotted against D^* across 24 printing conditions, with distinct alignment regimes based on AP. (C) Experimental data and theoretical fits using Eq. (8) for D^* as a function of E for different values of d_{nozzle}. (D) Schematic of fiber alignment regimes for different velocity ratios (V^*), where V^* is the ratio of ink extrusion speed from the nozzle (C) to the translational speed of the printbed (F). (E) Alignment parameter (AP) plotted against V^* for 24 printing conditions, with distinct alignment regimes based on AP. (F) Theoretical values of V^* plotted as a function of E for different values of d_{nozzle} and E. Data points denote the 24 experimental conditions that were tested for experimental validation of the fiber alignment regimes. (A, B, C, E, F) Data are mean ± standard deviation, $N = 3$ independent printing trials. $^{**}p < 0.01$,$^{***}p < 0.001$,$^{****}p < 0.0001$. (For interpretation of the references to color in this figure legend, the reader is referred to the web version of this article.)

where η is the apparent shear viscosity, we can get an expression for C:

$$C = \frac{4n}{3n+1} \cdot \frac{d_{nozzle}^2 \Delta P}{32 \eta L} \tag{14}$$

For our specific extrusion-based 3D printer, the theoretical equation for V^* is derived using mass conservation by equating the volumetric flow rate inside the syringe to the volumetric flow rate at the tip of the printing nozzle (supplemental equations S1 – S6) and can be expressed as:

$$V^* = \frac{4 A_{syringe} E}{\pi d_{nozzle}^2 \Delta x} \tag{15}$$

To confirm that this formulation of V^* can directly predict the direction of fiber alignment without any fitting parameters, we correlated the resulting theoretical V^* values with the experimentally determined alignment parameter (AP) across the range of E and d_{nozzle} conditions presented earlier (Fig. 4(E)). As before, we used our AP cutoff values to identify the regimes that correspond to perpendicular, random, and parallel fiber alignment. From this analysis, we observed that $V^* \leq 0.5$ results in parallel fibers ($AP \leq 0.5$), intermediate values of V^* ($0.5 < V^* \leq 1$) result in randomly aligned fibers ($0.5 < AP \leq 2$), and ($V^* > 1$) results in perpendicular fibers ($AP > 2$). These results agree with a similar ratio that was identified in earlier studies for an extrusion deposition additive manufacturing system (the ratio of the extrusion speed and print speed), where ratios less than unity resulted in greater fiber alignment in the printing direction [68].

To enable the prediction of fiber alignment with no fitting parameters, we plotted the theoretical curves of V^* as a function of E for each d_{nozzle} tested, using Eq. (15) (Fig. 4(F)). For ease of viewing, the three different fiber alignment regimes are shown as different color-coded regions, and we overlaid the points corresponding to the 24 specific combinations of E and d_{nozzle} tested experimentally. Thus, when increasing d_{nozzle} and keeping E constant, the fiber alignment will transition from perpendicular to parallel as V^* is decreasing. Similarly, when increasing the E and keeping the d_{nozzle} constant, the fiber alignment will transition from parallel to perpendicular as V^* is increasing. Thus, the parameter V^* provides a unified adjustment protocol for both piston displacement E and nozzle diameter d_{nozzle} to switch fiber alignment direction.

Similar plots could be constructed for other printer-ink combinations to enable prediction of printing parameters that result in specific fiber alignment orientations. As extrusion-based printers are generally widely available and easy to use, this framework could be readily adapted to other systems. While the diameter ratio (D^*) includes a fitting parameter that is related to the intrinsic ink properties, the velocity ratio (V^*) depends only on the printing parameters programmed into the 3D printer.

3.5. Control of fiber alignment in embedded 3D printing

Our data suggest that fiber alignment is primarily dictated by filament spreading versus filament drawing and does not depend on interactions between the filament and the printbed. To test this idea, we printed collagen filaments onto printbeds with differing levels of hydrophobicity (supplemental figure S10). Even though the advancing contact angle between the substrates was substantially different (55.40° and 172.53°), filaments printed with the same V^* had similar quantitative fiber alignment. Thus, we hypothesized that the same printing parameters that induce parallel or perpendicular fiber alignment when printed in air would also cause fiber alignment when printed into a support bath. Embedded 3D printing into support baths has emerged as a strategy to expand the range of printable materials and the complexity of fabricated structures with intricate features [69–71]. In contrast to printing in air, in embedded 3D printing the ink material is deposited into an aqueous yield-stress fluid [69]. This allows the printed material to remain suspended and supported during the printing process, enabling the creation of complex 3D structures that would otherwise collapse under their own weight and/or aqueous surface tension if printed in air [69].

To explore if our fiber alignment strategy could be extended to embedded 3D printing, we prepared a Carbopol support bath material.

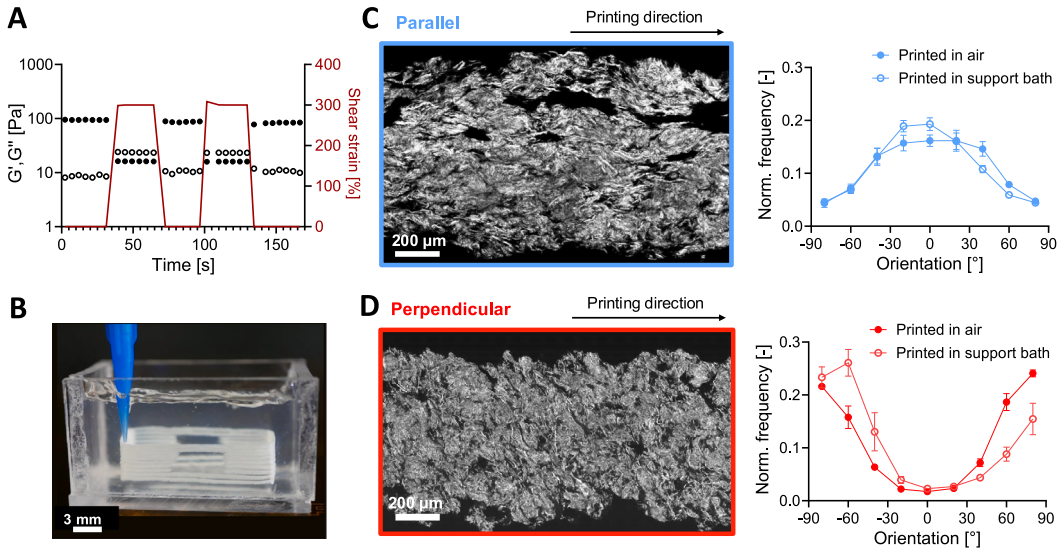

Fig. 5. Collagen fiber alignment in embedded 3D printing. (A) Shear rheology of Carbopol support bath upon alternating application of high (300%) or low (0.1%) shear strain (red line) demonstrates shear-thinning and self-healing behavior. Filled symbols correspond to storage moduli, G', and open symbols correspond to loss moduli, G''. (B) Multilayer collagen construct 3D printed in a Carbopol support bath. (C–D) (Left) Representative confocal reflectance images with parallel (C) and perpendicular (D) fiber alignment. (Right) Quantification of the collagen fiber alignment of collagen filaments printed in a Carbopol support bath compared to controls printed in air for similar V^* values. (C, D) The respective printing direction is shown for each alignment type (black arrow). (C, D) Data are mean ± standard deviation; $N = 3$ independent printing experiments. (For interpretation of the references to color in this figure legend, the reader is referred to the web version of this article.)

Carbopol is widely used as a support bath due to its self-healing behavior (Fig. 5(A)) [72]. In addition, previous work has demonstrated that a large range of printing speeds are compatible with Carbopol support baths without causing porosity in the final print [73].

As demonstration, we printed a 3D structure having hollow, suspended features (*i.e.* windows) and built up as a multilayered construct in which fiber alignment was tuned in each individual filament (Fig. 5(B)). In addition, single filaments, which allow for easier visualization of the collagen fibers after removal from the support bath, were printed with identical printing parameters (supplemental table S1). The fiber alignment of the resulting prints was imaged and quantified for comparison to that of filaments printed in air with the same printing conditions (Fig. 5(C,D)). Collagen fibers were well aligned when filaments were printed into the Carbopol support bath, both for conditions that result in parallel ($V^* \leq 0.5$) and perpendicular orientations ($V^* > 1$). Furthermore, the degree of fiber alignment was found to be similar for filaments printed in air or within the Carbopol support bath. For example, the AP for parallel alignment printing in air and in the support bath was found to be 0.35 ± 0.044 and 0.30 ± 0.020, respectively. The AP for perpendicular alignment in air and in the support bath was found to be 6.23 ± 0.750 and 9.57 ± 0.017, respectively. While printing in a support bath can produce filaments with both parallel and perpendicular fiber alignment, the inherent limitations and challenges of embedded 3D printing must also be considered when selecting printing parameters. For example, moving the printhead quickly ($V^* \leq 0.5$) can result in parallel fiber alignment, but this speed may also introduce print defects such as filament breakup, "crowning" (*i.e.* upwards flow of the ink material due to a prolonged crevice in the support bath), and extensive porosity [69,73–75]. Therefore, the printing parameter regimes for each alignment orientation will be affected by the viscosity ratio between the ink material and the support bath, which will need to be tuned for each material system.

3.6. Collagen fiber alignment guides cell orientation

To evaluate if patterned collagen fibers could influence cellular orientation, we seeded human corneal mesenchymal stromal cells (CMSCs) on collagen scaffolds with parallel, perpendicular, and random fiber alignments. The native cornea has multidirectional collagen fiber alignment, which is responsible for imparting its structural and functional properties [5,76–78], and CMSCs are one of the regenerative cell types found in these tissues [79–81]. Specimens were printed with parallel or perpendicular collagen fiber alignment, following the printing guidelines identified earlier (parallel: V^*= 0.22, d_{nozzle}= 1.55 mm; perpendicular: V^*= 2.98, d_{nozzle}= 0.42 mm), and a cast gel condition with random fiber alignment was included as a negative control. The collagen fibers in the three different conditions were imaged through confocal reflectance on day 0 prior to cell seeding (first column of Fig. 6(A)), and the fiber orientation was determined for each sample. At days 1, 3, and 5 after CMSC seeding, the cell morphology was visualized with a live cell cytoplasmic marker (calcein-AM) as shown in columns 2–7 of Fig. 6(A) and supplemental figure S11. Across all timepoints, cells remained highly viable (about 99%, supplemental figure S12) and reached confluence by day 5. Moreover, the collagen fiber orientation was retained during that time period (supplemental figure S13). Cell alignment was quantified by calculating orientation histograms from these images on days 1 and 3. Already by day 1, the quantified cell orientation matched with the underlying collagen fiber alignment across all three types of fiber patterns (Fig. 6(B–D)). This agreement in alignment orientation persisted at day 3, as quantitatively evaluated in Fig. 6(B–D). At day 5, increased cell–cell contact due to cell proliferation prevented automated identification of individual cell borders for orientation analysis; nonetheless, fiber-guided cell alignment was readily observed through qualitative inspection of the confocal fluorescence micrographs. Cell morphology was further analyzed by staining the cell nuclei (DAPI) and filamentous actin (phalloidin) along with the aldehyde dehydrogenase 3 family member A1 (ALDH-3A1), a marker for differentiating CMSCs (Fig. 6(A)) [82,83]. Across all three cases (perpendicular, parallel, and random fiber alignments), and all timepoints, cells were observed to elongate and align with the underlying substrate while maintaining their positive staining for ALDH-3A1. Thus, similar to reports by others, controlling the orientation of collagen fibers at the microscale allows control of the cell orientation [6,7,30], which we uniquely demonstrate here by inducing cells to align in both parallel and perpendicular orientations.

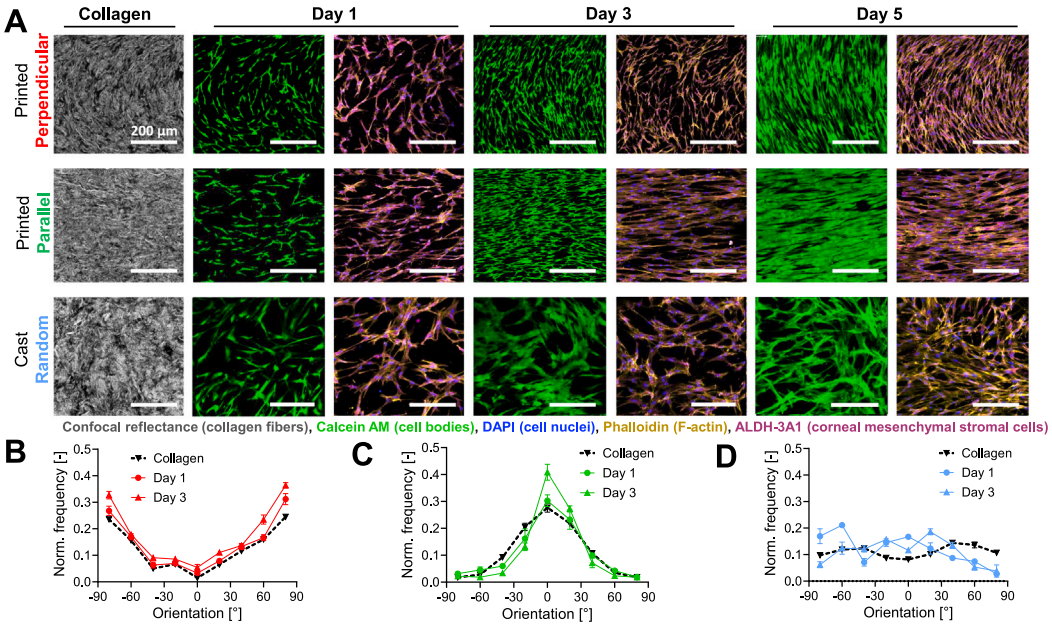

Fig. 6. Collagen fiber alignment guides cell orientation. (A) Representative confocal reflectance images of collagen fibers (gray) and confocal fluorescence images of CMSCs grown on the collagen filaments for 5 days and stained for cell bodies (green, calcein-AM), cell nuclei (blue, DAPI), filamentous actin (orange, phalloidin), and ALDH-3A1 (magenta). Printed samples included both perpendicular (top row) and parallel (middle row) collagen fiber alignment, and controls included cast samples (bottom row) with random fiber alignment. (B–D) Orientation of the collagen fibers and seeded cells on days 1 and 3 were quantified for the prints with perpendicular (B), parallel (C), and random (D) fiber alignments, normalized to the total count of fibers or cells, respectively. (For interpretation of the references to color in this figure legend, the reader is referred to the web version of this article.)

3.7. Dual-directional control of collagen fiber alignment in a single print

In native tissues, collagen fibers and endogenous cells are aligned in multiple directions within a single tissue [5,8,10–13]. Inspired by this, we reasoned that we should be able to modulate the printing conditions (*i.e.* V^*) during the fabrication process to achieve dual-directional collagen fiber alignment and hence different regions of cellular orientation within a single construct. Specimens with three different designs were created to demonstrate dual-directional control of alignment through either different interfilament or intrafilament fiber orientation patterning (Fig. 7(A)). In one type of interfilament patterning, sequential filaments can have alternating parallel and perpendicular fiber alignment. This can be achieved either (i) by using the same E but printing through two differently sized nozzles (left column, Fig. 7(A) and supplemental table S1) or (ii) by printing through the same nozzle (d_{nozzle} = constant) and varying E for sequential filaments (middle column, Fig. 7(A) and supplemental table S1). In our implementation, the first method was achieved by printing the filament with perpendicular alignment using a nozzle with a diameter of 0.16 mm at E = 0.007 mm. The nozzle was then manually replaced with a nozzle with a diameter of 1.55 mm, and the adjacent filament with parallel alignment was printed using the same E value. In the second approach, the nozzle diameter was kept constant and equal to 1.55 mm, and the alignment was modulated by changing the extrusion value, E, between filaments in the G-code by first printing a filament at E = 0.007 mm leading to parallel fiber alignment, followed by a filament printed at E = 0.040 mm leading to perpendicular fiber alignment. These strategies allow dynamic modulation of fiber orientation without altering the printhead path.

In intrafilament patterning, alternating regions of parallel and perpendicular fiber alignment are present in the same filament. This can be achieved using a single nozzle by varying E during continuous printing of a filament (right column, Fig. 7(A) and supplemental table S1). Specifically, the transition from parallel to perpendicular fiber orientation was achieved by keeping the nozzle diameter constant (d_{nozzle} = 1.55 mm) and programming the G-code to extrude at E = 0.007 mm for the first 1 cm of the filament and then increasing it to E = 0.04 mm for the following 1 cm. This *in situ* modulation of E during continuous extrusion enabled a seamless transitions in fiber orientation within a single filament.

CMSCs were seeded onto these three different dual-directional fiber alignment prints, and cell morphology was visualized through cytoplasmic calcein-AM staining on day 3. Cellular orientation was digitally analyzed and color coded to identify cells with parallel (blue, −45° to 45°,) or perpendicular alignment (red, −90° to −45° and 45° to 90°) relative to the printing direction (Fig. 7(B)). Cells appeared to adhere equally well on construct regions with parallel or perpendicular fiber alignment, (Fig. 7(C)). As expected, cells followed the alignment of the underlying collagen fibers, as visualized by automated color coding (Fig. 7(D)) and by quantitative analysis (Fig. 7(E)). Thus, this technique offers the flexibility to create dual-directional patterns of fiber alignment using either a multiple nozzle printer (by altering d_{nozzle} and keeping E constant) or a single nozzle printer (by altering E and keeping d_{nozzle} constant). This versatile approach will enable the fabrication of printed constructs with control over different regions of patterned cell orientation to mimic native tissue architecture.

4. Conclusion

Control over fiber alignment in engineered scaffolds is essential to accurately emulate natural tissue. Here, we demonstrate an extrusion-based 3D printing approach to control collagen fiber orientation in two independent directions by tuning the printing parameters. Importantly, CMSCs cultured on the printed collagen scaffolds were found to orient along the direction of the patterned collagen fibers across multiple days. While here we used plunger-controlled 3D printing, the same principles should be applicable to other types of extrusion-based 3D printing, such as a pressure-controlled setup [84]. The key insight is that post-extrusion fluid movement of the ink can induce alignment of embedded fibers. When the printing parameters are selected so that the ink undergoes lateral filament spreading, the fibers can align perpendicular to the printing direction. In contrast, when the printing

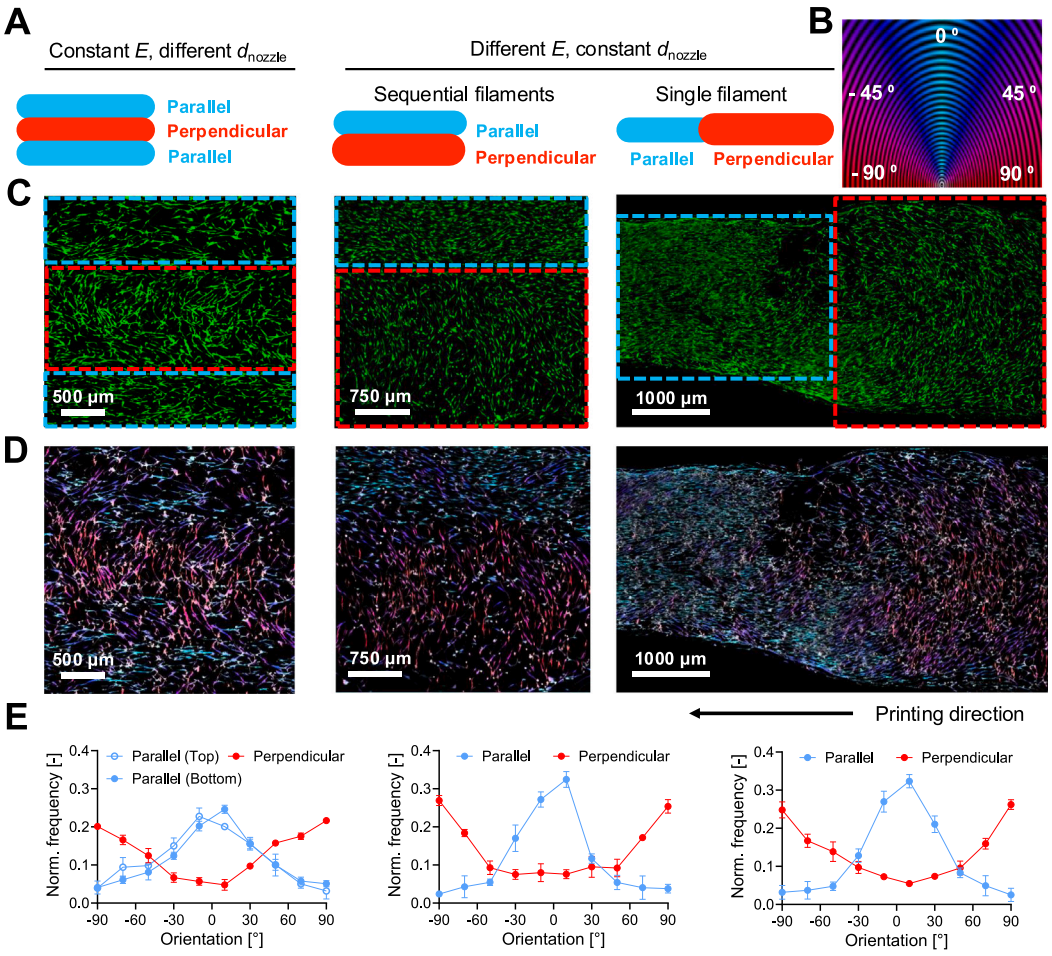

Fig. 7. Dual-directional control of fiber and cell alignment in a single print. (A) Schematic of designs used to achieve dual-directional collagen fiber alignment in a single print, where the blue and red colors refer to regions printed with V^* values shown to result in a parallel and perpendicular alignment, respectively. (B) Color code used for automated analysis of cell orientation, relative to the printing direction (0°). (C) Representative confocal images of CMSCs cultured on top of the collagen prints, visualized through calcein-AM. (D) Representative images of cell morphology with automated coloring based on their orientation using the legend from panel B. (E) Histograms of cell orientation for the different regions of each design, normalized to the total cell count. (For interpretation of the references to color in this figure legend, the reader is referred to the web version of this article.)

parameters are selected so that the ink undergoes extensional drawing, the fibers will align parallel to the printing direction. Using conservation of mass principles and automated quantification of fiber alignment, we were able to identity the printing parameters that reliably produce parallel, random, and perpendicular fiber patterns. Specifically, we identified V^* (the speed of ink extrusion from the nozzle relative to the translational speed of the printhead) as being able to directly modify D^* (the filament diameter normalized to the nozzle diameter), and hence control fiber alignment. From Eqs. (8) and (15), V^* is related to D^* as:

$$D^* = \sqrt{\beta\, V^*}, \tag{16}$$

where β is a material-specific constant that will likely depend on intrinsic ink properties such as extensional viscosity. For the high concentration collagen ink used in this study, we experimentally determined $\beta \approx 4.49 \pm 0.031$. Future work to identify the range of ink properties that are compatible with this fiber alignment strategy may allow extension to other types of fibrous inks. For example, our 3D printing alignment strategy could be applied to other fibrous or anisotropic materials, such as cellulose nanofibers, filamentous bacteriophages, or composites of fibrous and amorphous collagen inks [85–87], which would likely have distinct β constants. Moreover, the alignment of collagen fibers is expected to also affect the mechanical properties, such as Young's modulus, tensile strength, and strain at break, of the printed constructs. In particular, the anisotropy of the fiber orientation is expected to cause different mechanical properties parallel and perpendicular to the direction of fiber alignment. In general, materials with aligned fibers show increased load-bearing capability along the alignment direction [88–93].

The test structures printed here were limited primarily to planar constructs, as this allowed for easy visualization and quantification of fiber alignment. Layer-by-layer extrusion printing has been successfully used to fabricate a wide variety of different 3D constructs with more complex geometric features. As a first step towards this goal, we demonstrated that lateral filament spreading and extensional filament drawing can both be achieved within a support bath to induce successful fiber alignment in the perpendicular and parallel directions, respectively. Future work could build on these proof-of-concept experiments to fabricate structures with more complex 3D shapes that have different fiber alignment patterns in different regions of the tissue. Interlayer bonding and fiber alignment in multilayer structures remain challenges in the field and are highly active areas of research [94,95]. Systematic studies investigating the balance between crosslinking kinetics, layer stiffness, and interlayer bonding will therefore be critical for translating this strategy towards more complex, multilayered architectures. Furthermore, multiplexing this extrusion-based printing strategy with other printing modalities would open up further possibilities to achieve biomimetic structures. Moreover, while here we demonstrate control over two fiber orientations (parallel or perpendicular), some tissues have multiple fiber orientations present. Thus, future studies could

explore methods to further refine the alignment process to achieve greater orientational precision.

Here, we demonstrate that the patterned fibrous structures were able to induce cellular alignment of the seeded CMSCs, which was maintained over five days. Cell morphology is known to correlate with a number of changes in cell phenotype, and future studies could explore how the fibrous patterns might impact cell proliferation and migration rates, in addition to possible changes in protein expression. Importantly, this fabrication platform provides a framework for future investigations into how controlled spatial patterning of dual-directional collagen fibers can direct cell migration and tissue-level organization. Moreover, a great deal of other cell types have been reported to respond to aligned fibrous structures, including endothelial cells, neurons, and myoblasts, to name only a few [24,32,33,36,96–98]. Thus the 3D printing strategy demonstrated here could be readily extended to a wide range of other cell types. For our studies, cells were seeded onto the surfaces of pre-fabricated constructs; therefore, it remains to be explored if cells could also be directly incorporated into the ink prior to printing to formulate a living bioink. Our collagen ink is already at physiological pH inside the print cartridge; thus, the ink material is cell compatible. On the other hand, the presence of cells may significantly alter the viscoelastic ink properties, which may interfere with fiber alignment. Alternative strategies might include separate printing of an acellular collagen ink and a cellular ink using two print nozzles, as has been previously demonstrated for embedded printing [42,99]. Here, we used a relatively high print speed to be consistent with other published work on fiber alignment printing [100,101]. While this rapid print speed improves experimental throughput, it may inhibit the printing of cell-laden bioinks. Future work can explore the use of our V^* model to predict parallel and perpendicular fiber orientations at other print speeds and their extension to cell-laden bioinks. Moreover, combinatorial approaches utilizing a blend of fibrous and amorphous collagen networks as shown in our earlier work can be used, with the aim of achieving more transparent specimens similar to the cornea [87,102]. Another open question for future study is to evaluate if fiber alignment and cellular orientation are stable after *in vivo* implantation.

In summary, this work demonstrates a theoretical and experimental framework to achieve the reproducible fabrication of 3D printed structures with controlled collagen fiber patterns. This technique can be used to achieve different patterns of collagen fiber alignment within different regions of a fabricated construct. These patterns of fiber alignment then induce cell orientation along pre-determined directions. This dual-directional fiber alignment strategy greatly expands the design space for 3D printing of complex, biomimetic tissues.

CRediT authorship contribution statement

Diya Singhal: Writing – review & editing, Writing – original draft, Visualization, Methodology, Investigation, Formal analysis, Data curation, Conceptualization. **Fotis Christakopoulos:** Writing – review & editing, Writing – original draft, Visualization, Supervision, Methodology, Investigation, Formal analysis, Data curation, Conceptualization. **Lucia G. Brunel:** Writing – review & editing, Methodology, Investigation, Conceptualization. **Suraj Borkar:** Writing – review & editing, Methodology, Investigation. **Vanessa M. Doulames:** Writing – review & editing, Methodology, Investigation. **Esther A.T. Mozipo:** Investigation, Data curation. **David Myung:** Writing – review & editing, Supervision, Funding acquisition, Conceptualization. **Gerald G. Fuller:** Writing – review & editing, Supervision, Conceptualization. **Sarah C. Heilshorn:** Writing – review & editing, Supervision, Resources, Project administration, Funding acquisition, Conceptualization.

Declaration of competing interest

The authors declare that they have no known competing financial interests or personal relationships that could have appeared to influence the work reported in this paper.

The author is an Editorial Board Member/Editor-in-Chief/Associate Editor/Guest Editor for this journal and was not involved in the editorial review or the decision to publish this article

Acknowledgments

The authors thank Betty Cai and Dr. David Kilian for helpful discussions and Dr. Annika Enejder for assistance with the SHG measurements. The authors acknowledge funding support from the Stanford Graduate Fellowship in Science and Engineering (D.S.), the Swiss National Science Foundation P500PN210723 (F.C.), the National Institutes of Health including R01-EY035697 (S.C.H., D.M.), R01EY033363 (D.M.), F31-EY034785 (L.G.B), K01-EB033870 (V.M.D.), and T32 Biotechnology Training Program (E.M.), the National Science Foundation including DMR-2427971 (S.C.H.) and DGE-2146755 (E.M.), and the ARCS Foundation Scholarship (L.G.B.). Additional support was provided through departmental core grants from Research to Prevent Blindness and the National Eye Institute P30EY026877 (D.M.). Part of this work was performed at the Stanford Nano Shared Facilities, supported by the NSF under award ECCS-2026822.

Appendix A. Supplementary data

Supplementary material related to this article can be found online at https://doi.org/10.1016/j.actbio.2025.11.013.

Data availability

All data needed to evaluate the conclusions in the paper are present in the paper and/or the Supplementary data. Data have also been deposited in the Stanford Digital Repository and can be accessed through the persistent URL (https://purl.stanford.edu/bw985nr0021) and the DOI (https://doi.org/10.25740/bw985nr0021).

References

[1] Xianyan Wang, Hyeon Joo Kim, Cheryl Wong, Charu Vepari, Akira Matsumoto, David L. Kaplan, Fibrous proteins and tissue engineering, Mater. Today 9 (12) (2006) 44–53.

[2] Szabolcs Suveges, Ibrahim Chamseddine, Katarzyna A. Rejniak, Raluca Eftimie, Dumitru Trucu, Collective Cell Migration in a Fibrous Environment: A Hybrid Multiscale Modelling Approach, Front. Appl. Math. Stat. 7 (2021) 680029.

[3] Rebecca M. Crossley, Samuel Johnson, Erika Tsingos, Zoe Bell, Massimiliano Berardi, Margherita Botticelli, Quirine J.S. Braat, John Metzcar, Marco Ruscone, Yuan Yin, Robyn Shuttleworth, Modeling the extracellular matrix in cell migration and morphogenesis: a guide for the curious biologist, Front. Cell Dev. Biol. 12 (2024) 1354132.

[4] John E. Kirkwood, Gerald G. Fuller, Liquid crystalline collagen: A self-assembled morphology for the orientation of mammalian cells, Langmuir 25 (5) (2009) 3200–3206.

[5] Andrew J. Quantock, Moritz Winkler, Geraint J. Parfitt, Robert D. Young, Donald J. Brown, Craig Boote, James V. Jester, From nano to macro: Studying the hierarchical structure of the corneal extracellular matrix, Exp. Eye Res. 133 (2015) 81–99.

[6] Jiranuwat Sapudom, Shaza Karaman, Brian Chesney Quartey, Walaa Kamal El-din Mohamed, Nick Mahtani, Anna Garcia-Sabaté, Jeremy Teo, Collagen Fibril Orientation Instructs Fibroblast Differentiation Via Cell Contractility, Adv. Sci. 10 (22) (2023) 2301353.

[7] Hyeonji Kim, Jinah Jang, Junshin Park, Kyoung Pil Lee, Seunghun Lee, Dong Mok Lee, Ki Hean Kim, Hong Kyun Kim, Dong Woo Cho, Shear-induced alignment of collagen fibrils using 3D cell printing for corneal stroma tissue engineering, Biofabrication 11 (2019) 035017.

[8] Jie Liu, Ming you Xu, Jing Wu, Hao Zhang, Li Yang, Deng xing Lun, Yong cheng Hu, Bin Liu, Picrosirius-Polarization Method for Collagen Fiber Detection in Tendons: A Mini-Review, Orthop. Surg. 13 (3) (2021) 701–707.

[9] Alexandra S. Piotrowski-Daspit, Bryan A. Nerger, Abraham E. Wolf, Sankaran Sundaresan, Celeste M. Nelson, Dynamics of Tissue-Induced Alignment of Fibrous Extracellular Matrix, Biophys. J. 113 (3) (2017) 702–713.

[10] Egor Olegovich Osidak, Vadim Igorevich Kozhukhov, Mariya Sergeevna Osidak, Sergey Petrovich Domogatsky, Collagen as bioink for bioprinting: A comprehensive review, Int. J. Bioprinting 6 (3) (2020) 270.

[11] Yiyu Wang, Zhengke Wang, Yan Dong, Collagen-Based Biomaterials for Tissue Engineering, ACS Biomater. Sci. Eng. 9 (3) (2023) 1132–1150.

[12] Jet R. Peters, Marit Hoogenboom, Florencia Abinzano, Sebastien J.P. Callens, Jasper Foolen, Keita Ito, Tissue growth as a mechanism for collagen fiber alignment in articular cartilage, Sci. Rep. 14 (2024) 31121.

[13] Shannon L.M. Dahl, Megann E. Vaughn, Laura E. Niklason, An ultrastructural analysis of collagen in tissue engineered arteries, Ann. Biomed. Eng. 35 (2007) 1749–1755.

[14] David F. Holmes, Christopher J. Gilpin, Clair Baldock, Ulrike Ziese, Abraham J. Koster, Karl E. Kadler, Corneal collagen fibril structure in three dimensions: Structural insights into fibril assembly, mechanical properties, and tissue organization, Proc. Natl. Acad. Sci. 98 (2001) 7307–7312.

[15] Robert E. Shadwick, Mechanical Design in Arteries, J. Exp. Biol. 202 (1999) 3305–3313.

[16] Joseph M. Szulczewski, David R. Inman, Maria Proestaki, Jacob Notbohm, Brian M. Burkel, Suzanne M. Ponik, Directional cues in the tumor microenvironment due to cell contraction against aligned collagen fibers, Acta Biomater. 129 (2021) 96–109.

[17] Andrew Clark, Ananyo Maitra, Cécile Jacques, Martin Bergert, Carlos Pérez-González, Anthony Simon, Luc Lederer, Alba Diz-Muñoz, Xavier Trepat, Raphaël Voituriez, Danijela Vignjevic, Self-generated gradients steer collective migration on viscoelastic collagen networks, Nat. Mater. 21 (2022) 1–11.

[18] Qihui Fan, Yu Zheng, Xiaochen Wang, Ruipei Xie, Yu Ding, Boyi Wang, Xiaoyu Yu, Ying Lu, Liyu Liu, Yunliang Li, Ming Li, Yuanjin Zhao, Yang Jiao, Fangfu Ye, Dynamically re-organized collagen fiber bundles transmit mechanical signals and induce strongly correlated cell migration and self-organization, Angew. Chem. Int. Ed. 60 (21) (2021) 11858–11867.

[19] Cheol Ho Heo, Ki Baek Yeo, Minjung Chae, Seon Young Bak, Hyeon Jin Choi, Sohyeon Jeong, Nakwon Choi, Seung-Kyun Kang, Sang Ho Jun, Myoung-Ryul Ok, So Yeon Kim, Spontaneous bone regeneration achieved through one-step alignment of human mesenchymal stem cell-embedded collagen, Acta Biomater. 196 (2025) 136–151.

[20] Shaohua Wu, Hao Peng, Xiuhong Li, Philipp N. Streubel, Yong Liu, Bin Duan, Effect of scaffold morphology and cell co-culture on tenogenic differentiation of HADMSC on centrifugal melt electrospun poly (Llactic acid) fibrous meshes, Biofabrication 9 (2017) 044106.

[21] Jian Xie, Hangqi Shen, Guangyin Yuan, Kaili Lin, Jiansheng Su, The effects of alignment and diameter of electrospun fibers on the cellular behaviors and osteogenesis of BMSCs, Mater. Sci. Eng.: C 120 (2021) 111787.

[22] Shawn P. Carey, Zachary E. Goldblatt, Karen E. Martin, Bethsabe Romero, Rebecca M. Williams, Cynthia A. Reinhart-King, Local extracellular matrix alignment directs cellular protrusion dynamics and migration through Rac1 and FAK, Integr. Biol. (United Kingdom) 8 (2016) 821–835.

[23] Dandan Pei, Mengqi Wang, Wenfang Li, Meiwen Li, Qian Liu, Rui Ding, Jing Zhao, Ang Li, Jing Li, Feng Xu, Guorui Jin, Remodeling of aligned fibrous extracellular matrix by encapsulated cells under mechanical stretching, Acta Biomater. 112 (2020) 202–212.

[24] Shawn H. Lim, Xingyu Y. Liu, Hongjun Song, Kevin J. Yarema, Hai Quan Mao, The effect of nanofiber-guided cell alignment on the preferential differentiation of neural stem cells, Biomaterials 31 (34) (2010) 9031–9039.

[25] Animesh Agrawal, Bae Hoon Lee, Scott A. Irvine, Jia An, Ramya Bhuthalingam, Vaishali Singh, Kok Yao Low, Chee Kai Chua, Subbu S. Venkatraman, Smooth muscle cell alignment and phenotype control by melt spun polycaprolactone fibers for seeding of tissue engineered blood vessels, Int. J. Biomater. 2015 (1) (2015) 434876.

[26] Bryan A. Nerger, P.T. Brun, Celeste M. Nelson, Microextrusion printing cell-laden networks of type i collagen with patterned fiber alignment and geometry, Soft Matter 15 (28) (2019) 5728–5738.

[27] Alysha P. Kishan, Andrew B. Robbins, Sahar F. Mohiuddin, Mingliang Jiang, Michael R. Moreno, Elizabeth M. Cosgriff-Hernandez, Fabrication of macromolecular gradients in aligned fiber scaffolds using a combination of in-line blending and air-gap electrospinning, Acta Biomater. 56 (2017) 118–128.

[28] Nicolas Builles, Hélène Janin-Manificat, Marilyne Malbouyres, Virginie Justin, Marie Rose Rovère, Graziella Pellegrini, Jim Torbet, David J.S. Hulmes, Carole Burillon, Odile Damour, Florence Ruggiero, Use of magnetically oriented orthogonal collagen scaffolds for hemi-corneal reconstruction and regeneration, Biomaterials 31 (2010) 8313–8322.

[29] Adeel Ahmed, Mehran Mansouri, Indranil M. Joshi, Ann M. Byerley, Steven W. Day, Thomas R. Gaborski, Vinay V. Abhyankar, Local extensional flows promote long-range fiber alignment in 3D collagen hydrogels, Biofabrication 14 (2022) 035019.

[30] Kristin M. Riching, Benjamin L. Cox, Max R. Salick, Carolyn Pehlke, Andrew S. Riching, Susan M. Ponik, Benjamin R. Bass, Wendy C. Crone, Yi Jiang, Alissa M. Weaver, Kevin W. Eliceiri, Patricia J. Keely, 3D collagen alignment limits protrusions to enhance breast cancer cell persistence, Biophys. J. 107 (11) (2015) 2546–2558.

[31] Indranil M. Joshi, Mehran Mansouri, Adeel Ahmed, Dinindu De Silva, Richard A. Simon, Poorya Esmaili, Danielle E. Desa, Tresa M. Elias, Edward B. Brown, Vinay V. Abhyankar, Microengineering 3D collagen matrices with tumor-mimetic gradients in fiber alignment, Adv. Funct. Mater. 34 (2024) 2308071.

[32] Erfan Soliman, Fabio Bianchi, James N. Sleigh, Julian H. George, M. Zameel Cader, Zhanfeng Cui, Hua Ye, Aligned electrospun fibers for neural patterning, Biotechnol. Lett. 40 (3) (2018) 601–607.

[33] Mei Yang, Qichao Cheng, Guanshan Zhou, Tiancheng Wei, Suting Zhong, Leihao Lu, Chi Yan, Yecheng Wang, Mingzheng Fang, Mingying Yang, Weidong Ping, Electrospinning Aligned SF/Magnetic Nanoparticles-Blend Nanofiber Scaffolds for Inducing Skeletal Myoblast Alignment and Differentiation, ACS Appl. Bio Mater. 7 (11) (2024) 7710–7718.

[34] Xiaoqian Qian, Xiangming Zhou, Bin Mu, Zongjin Li, Fiber alignment and property direction dependency of FRC extrudate, Cem. Concr. Res. 33 (10) (2003) 1575–1581.

[35] Henk R. Hoogenkamp, Gert Jan Bakker, Louis Wolf, Patricia Suurs, Bertus Dunnewind, Shai Barbut, Peter Friedl, Toin H. Van Kuppevelt, Willeke F. Daamen, Directing collagen fibers using counter-rotating cone extrusion, Acta Biomater. 12 (2015) 113–121.

[36] Michael G. McCoy, Jane M. Wei, Siyoung Choi, Julian Palacios Goerger, Warren Zipfel, Claudia Fischbach, Collagen Fiber Orientation Regulates 3D Vascular Network Formation and Alignment, ACS Biomater. Sci. Eng. 4 (8) (2018) 2967–2976.

[37] Bryan A. Nerger, P.T. Brun, Celeste M. Nelson, Marangoni flows drive the alignment of fibrillar cell-laden hydrogels, Sci. Adv. 6 (24) (2020) eaaz7748.

[38] Mark A. Skylar-Scott, Sebastien G.M. Uzel, Lucy L. Nam, John H. Ahrens, Ryan L. Truby, Sarita Damaraju, Jennifer A. Lewis, Biomanufacturing of organ-specific tissues with high cellular density and embedded vascular channels, Sci. Adv. 5 (9) (2019) eaaw2459.

[39] Jonathan A. Brassard, Mike Nikolaev, Tania Hübscher, Moritz Hofer, Matthias P. Lutolf, Recapitulating macro-scale tissue self-organization through organoid bioprinting, Nat. Mater. 20 (2021) 22–29.

[40] Tetsuya Imamura, Mitsuru Shimamura, Teruyuki Ogawa, Tomonori Minagawa, Takashi Nagai, Sudha Silwal Gautam, Osamu Ishizuka, Biofabricated Structures Reconstruct Functional Urinary Bladders in Radiation-Injured Rat Bladders, Tissue Eng. - Part A 24 (21–22) (2018) 1574–1587.

[41] A. Lee, A.R. Hudson, D.J. Shiwarski, J.W. Tashman, T.J. Hinton, S. Yerneni, J.M. Bliley, P.G. Campbell, A.W. Feinberg, 3D bioprinting of collagen to rebuild components of the human heart, Science 365 (6452) (2019) 482–487.

[42] Daniel J. Shiwarski, Andrew R. Hudson, Joshua W. Tashman, Ezgi Bakirci, Samuel Moss, Brian D. Coffin, Adam W. Feinberg, 3D bioprinting of collagen-based high-resolution internally perfusable scaffolds for engineering fully biologic tissue systems, Sci. Adv. 11 (17) (2025) eadu5905.

[43] Giovanna Ricci, Filippo Gibelli, Ascanio Sirignano, Three-Dimensional Bioprinting of Human Organs and Tissues: Bioethical and Medico-Legal Implications Examined through a Scoping Review, Bioengineering 10 (2023) 1052.

[44] Michelle S. Huang, Fotis Christakopoulos, Julien G. Roth, Sarah C. Heilshorn, Organoid bioprinting: from cells to functional tissues, Nat. Rev. Bioeng. 3 (2025) 126–142.

[45] Sean V. Murphy, Anthony Atala, 3D bioprinting of tissues and organs, Nature Biotechnol. 32 (2014) 773–785.

[46] A. Peterlin, Drawing and extrusion of semi-crystalline polymers, Colloid Polym. Sci. 265 (5) (1987) 357–382.

[47] Kazuo Nakayama, Hisaaki Kanetsuna, Hydrostatic extrusion of solid polymers - Part 5 Structure and molecular orientation of extruded polyethylene, J. Mater. Sci. 10 (1975) 1105–1118.

[48] Salim A. Ghodbane, N. Sanjeeva Murthy, Michael G. Dunn, J. Kohn, Achieving molecular orientation in thermally extruded 3D printed objects, Biofabrication 11 (2019) 045004.

[49] Tim Heitkamp, Sebastian Kuschmitz, Simon Girnth, Justin Dean Marx, Günter Klawitter, Nils Waldt, Thomas Vietor, Stress-adapted fiber orientation along the principal stress directions for continuous fiber-reinforced material extrusion, Prog. Addit. Manuf. 8 (3) (2023) 541–559.

[50] Fotis Christakopoulos, Stephan P. Busato, Enrico M. Troisi, Xiang Kong, Nic Friederichs, Theo A. Tervoort, Solid-state extrusion of nascent disentangled ultra-high molecular weight polyethylene, Polym. Eng. Sci. 64 (8) (2024) 3606–3616.

[51] James P. Lewicki, Jennifer N. Rodriguez, Cheng Zhu, Marcus A. Worsley, Amanda S. Wu, Yuliya Kanarska, John D. Horn, Eric B. Duoss, Jason M. Ortega, William Elmer, Ryan Hensleigh, Ryan A. Fellini, Michael J. King, 3D-Printing of Meso-structurally Ordered Carbon Fiber/Polymer Composites with Unprecedented Orthotropic Physical Properties, Sci. Rep. 7 (2017) 43401.

[52] Kira Pusch, Thomas J. Hinton, Adam W. Feinberg, Large volume syringe pump extruder for desktop 3D printers, HardwareX 3 (2018) 49–61.

[53] Sarah M. Hull, Junzhe Lou, Christopher D. Lindsay, Renato S. Navarro, Betty Cai, Lucia G. Brunel, Ashley D. Westerfield, Yan Xia, Sarah C. Heilshorn, 3D bioprinting of dynamic hydrogel bioinks enabled by small molecule modulators, Sci. Adv. 9 (13) (2023) eade7880.

[54] Sayena Jabbehdari, Ghasem Yazdanpanah, Levi N. Kanu, Khandaker N. Anwar, Xiang Shen, Behnam Rabiee, Ilham Putra, Medi Eslani, Mark I. Rosenblatt, Peiman Hematti, Ali R. Djalilian, Reproducible derivation and expansion of corneal mesenchymal stromal cells for therapeutic applications, Transl. Vis. Sci. Technol. 9 (3) (2020) 26.

[55] Jeremy S. Bredfeldt, Yuming Liu, Carolyn A. Pehlke, Matthew W. Conklin, Joseph M. Szulczewski, David R. Inman, Patricia J. Keely, Robert D. Nowak, Thomas R. Mackie, Kevin W. Eliceiri, Computational segmentation of collagen fibers from second-harmonic generation images of breast cancer, J. Biomed. Opt. 19 (1) (2014) 016007.

[56] Zhengwei Li, Changshun Ruan, Xufeng Niu, Collagen-based bioinks for regenerative medicine: Fabrication, application and prospective, Med. Nov. Technol. Devices 17 (37) (2023) 100211.

[57] Samuel P. Moss, Daniel J. Shiwarski, Adam W. Feinberg, FRESH 3D Bioprinting of Collagen Types I, II, and III, ACS Biomater. Sci. Eng. 11 (1) (2025) 556–563.

[58] Fengzhi Jiang, Heinrich Hörber, Jonathon Howard, Daniel J. Müller, Assembly of collagen into microribbons: Effects of pH and electrolytes, J. Struct. Biol. 148 (3) (2004) 268–278.

[59] Charles C. Banos, Amelia H. Thomas, Catherine K. Kuo, Collagen fibrillogenesis in tendon development: Current models and regulation of fibril assembly, Birth Defects Res. Part C - Embryo Today: Rev. 84 (3) (2008) 228–244.

[60] Ming Fang, Elizabeth L. Goldstein, Eryn K. Matich, Bradford G. Orr, Mark M. Banaszak Holl, Type i collagen self-assembly: The roles of substrate and concentration, Langmuir 29 (7) (2013) 2330–2338.

[61] Eesha Khare, Chi Hua Yu, Constancio Gonzalez Obeso, Mario Milazzo, David L. Kaplan, Markus J. Buehler, Discovering design principles of collagen molecular stability using a genetic algorithm, deep learning, and experimental validation, Proc. Natl. Acad. Sci. USA 119 (40) (2022) 2209524119.

[62] Mengfan Lou, Zhenyu Ouyang, Enhancing polymer fiber orientation with 3D-printed shell–core structures, J. Non-Newton. Fluid Mech. 335 (2025) 105352.

[63] Jingyuan Tang, Xi Chen, Fengkai Liu, Liangsong Zeng, Zhigang Suo, Jingda Tang, Why are soft collagenous tissues so tough? Sci. Adv. 11 (25) (2025) eadw0808.

[64] V.-P. Karjalainen, I. Kestilä, M.A. Finnilä, E. Folkesson, A. Turkiewicz, P. Önnerfjord, V. Hughes, J. Tjörnstrand, M. Englund, S. Saarakkala, Quantitative three-dimensional collagen orientation analysis of human meniscus posterior horn in health and osteoarthritis using micro-computed tomography, Osteoarthr. Cartil. 29 (5) (2021) 762–772.

[65] Woojin M. Han, Nandan L. Nerurkar, Lachlan J. Smith, Nathan T. Jacobs, Robert L. Mauck, Dawn M. Elliott, Multi-scale structural and tensile mechanical response of annulus fibrosus to osmotic loading, Ann. Biomed. Eng. 40 (7) (2012) 1610–1621.

[66] Jiongyi Yan, Emrah Demirci, Ajith Ganesan, Andrew Gleadall, Extrusion width critically affects fibre orientation in short fibre reinforced material extrusion additive manufacturing, Addit. Manuf. 49 (2022) 102496.

[67] Christopher W. Macosko, Rheology: Principles, Measurements, and Applications, Wiley-VCH, 1994.

[68] Pasita Pibulchinda, Eduardo Barocio, Anthony J. Favaloro, R. Byron Pipes, Influence of printing conditions on the extrudate shape and fiber orientation in extrusion deposition additive manufacturing, Compos. Part B: Eng. 261 (2023) 110793.

[69] Lucia G. Brunel, Sarah M. Hull, Sarah C. Heilshorn, Engineered assistive materials for 3D bioprinting: support baths and sacrificial inks, Biofabrication 14 (3) (2022) 032001.

[70] Malin Becker, Melvin Gurian, Maik Schot, Jeroen Leijten, Aqueous Two-Phase Enabled Low Viscosity 3D (LoV3D) Bioprinting of Living Matter, Adv. Sci. 10 (2023) 2204609.

[71] Shinji Sakai, Takahiro Morita, One-step FRESH bioprinting of low-viscosity silk fibroin inks, ACS Biomater. Sci. Eng. 8 (6) (2022) 2589–2597, PMID: 35608818.

[72] Tapomoy Bhattacharjee, Steven M. Zehnder, Kyle G. Rowe, Suhani Jain, Ryan M. Nixon, W. Gregory Sawyer, Thomas E. Angelini, Writing in the granular gel medium, Sci. Adv. 1 (8) (2015) e1500655.

[73] Lucia G. Brunel, Fotis Christakopoulos, David Kilian, Betty Cai, Sarah M. Hull, Sarah C. Heilshorn, Embedded 3D bioprinting of collagen inks into mikrogel baths to control hydrogel microstructure and cell spreading, Adv. Heal. Mater. 13 (2024) 2303325.

[74] Leanne M. Friedrich, Ross T. Gunther, Jonathan E. Seppala, Suppression of Filament Defects in Embedded 3D Printing, ACS Appl. Mater. Interfaces 14 (28) (2022) 32561–32578.

[75] Kyle J. Leblanc, Sean R. Niemi, Alexander I. Bennett, Kathryn L. Harris, Kyle D. Schulze, W. Gregory Sawyer, Curtis Taylor, Thomas E. Angelini, Stability of High Speed 3D Printing in Liquid-Like Solids, ACS Biomater. Sci. Eng. 2 (10) (2016) 1796–1799.

[76] David E. Birk, Peter Brückner, Collagens, suprastructures, and collagen fibril assembly, in: Robert P. Mecham (Ed.), The Extracellular Matrix: An Overview, Springer Berlin Heidelberg, Berlin, Heidelberg, 2011, pp. 77–115.

[77] Luca Salvatore, Nunzia Gallo, Maria Lucia Natali, Alberta Terzi, Alessandro Sannino, Marta Madaghiele, Mimicking the Hierarchical Organization of Natural Collagen: Toward the Development of Ideal Scaffolding Material for Tissue Regeneration, Front. Bioeng. Biotechnol. 9 (2021) 644595.

[78] Geraint J. Parfitt, Christian Pinali, Robert D. Young, Andrew J. Quantock, Carlo Knupp, Three-dimensional reconstruction of collagen-proteoglycan interactions in the mouse corneal stroma by electron tomography, J. Struct. Biol. 170 (2) (2010) 392–397.

[79] Sayan Basu, Andrew J. Hertsenberg, Martha L. Funderburgh, Michael K. Burrow, Mary M. Mann, Yiqin Du, Kira L. Lathrop, Fatima N. Syed-Picard, Sheila M. Adams, David E. Birk, James L. Funderburgh, Human limbal biopsy-derived stromal stem cells prevent corneal scarring, Sci. Transl. Med. 6 (266) (2014) 266ra172.

[80] Medi Eslani, Ilham Putra, Xiang Shen, Judy Hamouie, Asha Tadepalli, Khandaker N. Anwar, John A. Kink, Samaneh Ghassemi, Gaurav Agnihotri, Sofiya Reshetylo, Alireza Mashaghi, Reza Dana, Peiman Hematti, Ali R. Djalilian, Cornea-Derived Mesenchymal Stromal Cells Therapeutically Modulate Macrophage Immunophenotype and Angiogenic Function, Stem Cells 36 (5) (2018) 775–784.

[81] Lucia G. Brunel, Betty Cai, Sarah M. Hull, Uiyoung Han, Thitima Wungcharoen, Gabriella Maria Fernandes-Cunha, Youngyoon Amy Seo, Patrik K. Johansson, Sarah C. Heilshorn, David Myung, In situ UNIversal Orthogonal Network (UNION) bioink deposition for direct delivery of corneal stromal stem cells to corneal wounds, Bioact. Mater. 48 (2025) 414–430.

[82] Yiqin Du, Martha L. Funderburgh, Mary M. Mann, Nirmala SundarRaj, James L. Funderburgh, Multipotent stem cells in human corneal stroma, Stem Cells 23 (2005) 1266–1275.

[83] Ying Pei, Rose Y. Reins, Alison M. McDermott, Aldehyde dehydrogenase (ALDH) 3A1 expression by the human keratocyte and its repair phenotypes, Exp. Eye Res. 83 (5) (2006) 1063–1073.

[84] Yu Shrike Zhang, Ghazaleh Haghiashtiani, Tania Hübscher, Daniel J. Kelly, Jia Min Lee, Matthias Lutolf, Michael C. McAlpine, Wai Yee Yeong, Marcy Zenobi-Wong, Jos Malda, 3D extrusion bioprinting, Nat. Rev. Methods Prim. 1 (2021) 75.

[85] John Moohan, Sarah A. Stewart, Eduardo Espinosa, Antonio Rosal, Alejandro Rodríguez, Eneko Larrañeta, Ryan F. Donnelly, Juan Domínguez-Robles, Cellulose nanofibers and other biopolymers for biomedical applications. A review, Appl. Sci. (Switzerland) 10 (2020) 65.

[86] Narsimha Mamidi, Rubén Gutiérrez García, José Daniel Hernández Martínez, Camila Martínez Briones, Andrea Michelle Martínez Ramos, María Fernanda Leal Tamez, Braulio González Del Valle, Francisco Javier Macias Segura, Recent advances in designing fibrous biomaterials for the domain of biomedical, clinical, and environmental applications, ACS Biomater. Sci. Eng. 8 (9) (2022) 3690–3716, PMID: 36037103.

[87] Lucia G. Brunel, Chris M. Long, Fotis Christakopoulos, Betty Cai, Patrik K. Johansson, Diya Singhal, Annika Enejder, David Myung, Sarah C. Heilshorn, Interpenetrating networks of fibrillar and amorphous collagen promote cell spreading and hydrogel stability, Acta Biomater. 193 (2025) 128–142.

[88] Neil L. Hancox, Rayner M. Mayer, Mechanical properties of aligned fibre composites, in: Design Data for Reinforced Plastics, Springer, Dordrecht, 1994, pp. 96–132.

[89] Mahesh Gupta, K.K. Wang, Fiber orientation and mechanical properties of short-fiber-reinforced injection-molded composites: Simulated and experimental results, Polym. Compos. 14 (1993) 367–382.

[90] Yixiang Wang, Lingyun Chen, Cellulose nanowhiskers and fiber alignment greatly improve mechanical properties of electrospun prolamin protein fibers, ACS Appl. Mater. Interfaces 6 (2014) 1709–1718.

[91] M. Kamaraj, V. Vishnu Vardhan, K.S. Charan, M. Lalith Lochan, Effect of fibre alignment on mechanical properties of natural fibre reinforced polymer composites, in: IOP Conference Series: Materials Science and Engineering, vol. 912, IOP Publishing Ltd, 2020.

[92] Donggeun Lee, Jinhan Cho, Jeong Gon Son, Bongjun Yeom, Highly aligned aramid nanofibrillar nanocomposites for enhanced dynamic mechanical properties, Compos. Part B: Eng. 229 (2022) 109467.
[93] Upendra Sharan Gupta, Amit Dharkar, Mohit Dhamarikar, Arpit Choudhary, Dipanshu Wasnik, Pankaj Chouhan, Sudhir Tiwari, Rajeev Namdeo, Study on the effects of fiber orientation on the mechanical properties of natural fiber reinforced epoxy composite by finite element method, Mater. Today Proc. 45 (2021) 7885–7893.
[94] Guiting Liu, Zhangfan Ding, Qijuan Yuan, Huixu Xie, Zhipeng Gu, Multi-layered hydrogels for biomedical applications, Front. Chem. 6 (2018) 439.
[95] Rongnian Xu, Mutian Hua, Shuwang Wu, Shuanhong Ma, Yunlei Zhang, Liqiang Zhang, Bo Yu, Meirong Cai, Ximin He, Feng Zhou, Continuously growing multi-layered hydrogel structures with seamless interlocked interface, Matter 5 (2022) 634–653.
[96] Echoe M. Bouta, Connor W. McCarthy, Alexander Keim, Han Bing Wang, Ryan J. Gilbert, Jeremy Goldman, Biomaterial guides for lymphatic endothelial cell alignment and migration, Acta Biomater. 7 (3) (2011) 1104–1113.
[97] Peng Yuan Wang, Hung Te Yu, Wei Bor Tsai, Modulation of alignment and differentiation of skeletal myoblasts by submicron ridges/grooves surface structure, Biotechnol. Bioeng. 106 (2) (2010) 285–294.
[98] Kazunori Shimizu, Hideaki Fujita, Eiji Nagamori, Alignment of skeletal muscle myoblasts and myotubes using linear micropatterned surfaces ground with abrasives, Biotechnol. Bioeng. 103 (3) (2009) 631–638.
[99] María Puertas-Bartolomé, Małgorzata K. Włodarczyk-Biegun, Aránzazu del Campo, Blanca Vázquez-Lasa, Julio San Román, 3D printing of a reactive hydrogel bio-ink using a static mixing tool, Polymers 12 (9) (2020) 1986.
[100] Ludwik Lorkowski, Katarzyna Wybrzak, Emila Brancewicz-Steinmetz, Jacek Świniarski, Jacek Sawicki, Influence of print speed on the mechanical performance of 3D-printed bio-polymer polylactic acid, Materials 18 (8) (2025) 1765.
[101] Deian Dorel Ardeljan, Doina Frunzaverde, Vasile Cojocaru, Raul Rusalin Turiac, Nicoleta Bacescu, Costel Relu Ciubotariu, Gabriela Marginean, The impact of elevated printing speeds and filament color on the dimensional precision and tensile properties of FDM-printed PLA specimens, Polymers 17 (15) (2025) 2090.
[102] Lucia G. Brunel, Chris M. Long, Fotis Christakopoulos, Betty Cai, Narelli de Paiva Narciso, Patrik K. Johansson, Diya Singhal, Neil J. Baugh, Daiyao Zhang, Annika Enejder, David Myung, Sarah C. Heilshorn, Reinforcement of fibrillar collagen hydrogels with bioorthogonal covalent crosslinks, Biomacromolecules 26 (2025) 4404–4418.